Spectroscopy of core-excited molecules and exploration of the induced dynamics

Lindblom, Ville

2026

Spectroscopy of core-excited molecules and exploration of the induced dynamics

VILLE LINDBLOM
DEPARTMENT OF PHYSICS | FACULTY OF SCIENCE | LUND UNIVERSITY

Spectroscopy of core-excited molecules and exploration of the induced dynamics

Spectroscopy of core-excited molecules and exploration of the induced dynamics

by Ville Lindblom

LUND
UNIVERSITY

Thesis for the degree of Doctor of Philosophy

Thesis advisor: Prof. Stacey L. Sorensen
Faculty opponent: Prof. Arnaldo Naves de Brito

To be publicly defended, with the permission of the Faculty of Science of Lund University, at Lundmarksalen, Department of Physics, on Wednesday, the 20th of May 2026 at 13:15.

Organization	Document name
LUND UNIVERSITY Division of Synchrotron Radiation Research Box 124 SE–221 00 LUND Sweden	**DOCTORAL DISSERTATION** Date of disputation 2026-05-20 Sponsoring organization
Author(s) Ville Lindblom	

Title and subtitle

Spectroscopy of core-excited molecules and exploration of the induced dynamics

Abstract

This thesis investigates core excited electronic states of molecules in gas phase. In particular, the resonant transitions of ionised molecules, the site-selectivity surrounding Auger-Meitner decay, and the nuclear dynamics that may follow core excitation and ionisation.

Background: Fundamental understanding of molecules and ions lay the groundwork for all future applicative science and production. For example, explicit understanding of dissociative mechanisms leads to control of chemical reactions.

Aims: 1) To investigate molecular states after core photoexcitation in both molecules and ions. 2) To examine how the excited states decay through Auger-Meitner electron emission and how site-selectivity can be used to affect the decay rate. 3) To study the various nuclear geometrical changes (isomerisation, fragmentation or bond-elongation) for the excited/ionised states.

Methods: All the experiments done for this work utilised synchrotron radiation. The high resolution and frequency tunability are perfect for investigating resonant behaviours around the relevant energies (carbon K-edge). Three different experimental spectrometer types were used, an ion-trap with a reflectron mass spectrometer, hemispherical energy resolving electron analysers, and 3D momentum imaging spectrometers for charged particles.

Results: X-ray absorption like spectra were obtained for new ions, CH_3^+ ,CH_4^+, and CH_5^+. The ionised versions of CH_n revealed a much clearer picture of the various highly excited states which are not discernible in the neutral variant. The fluxional nature of CH_5^+ could be shown, as the spectrum was obtained from two geometrical structures.

The resonant Auger-Meitner decay spectra of ethyl trifluoroacetate (ESCA) and cyclohexadiene (CHD) revealed a clear state-selective process, and resonant behaviours.

The cyclic molecule cyclopropane showed different ring deforming dynamics dependent on which state was excited (σ^* or π^*). A specific dynamic in cyclopropane was also found, which was the roaming dissociation mechanism. The roaming was imaged with a 3D momentum spectrometer, and its existence was evident. This roaming motion leads to the formation of the H_3^+ ion.

Key words

Synchrotron radiation, multi-coincidence, fragmentation dynamics, molecular roaming, Ion spectroscopy, x-ray absorption spectroscopy, Photoelectron spectroscopy, Auger-Meitner decay

Classification system and/or index terms (if any)

Supplementary bibliographical information	Language
	English
ISSN and key title	ISBN
	978-91-8104-951-0 (print) 978-91-8104-952-7 (digital)
Recipient's notes	Number of pages: 206 / Price
	Security classification

Spectroscopy of core-excited molecules and exploration of the induced dynamics

by Ville Lindblom

LUND
UNIVERSITY

Doctoral Thesis

Faculty of Science, Division of Synchrotron Radiation Research

isbn: 978-91-8104-951-0 (print)
isbn: 978-91-8104-952-7 (pdf)

Printed in Sweden by Media-Tryck, Lund University, Lund 2026

Contents

List of papers

This thesis is based on the following publications and manuscripts, referred to by their Roman numerals:

Paper I:
Photoionisation of Methane Ions and Related Species

V. Lindblom, L. Kjellsson, R. Lindblad, J.E. Rubensson, V. Zamudio-Bayer, T. Lau, K. Hirsch, and S.L. Sorensen
In manuscript

I performed the data analysis of the experimental data, I made the theoretical calculations, and I wrote the manuscript.

Paper II:
Influence of Selective Carbon 1s Excitation on Auger-Meitner Decay in the ESCA Molecule

A. E. A. Fouda, **V. Lindblom**, S. H. Southworth, G. Doumy, P. J. Ho, L. Young, L. Cheng, and S. L. Sorensen
J. Phys. Chem. Lett. 2024, 15, 4286-4293

I took part in preparing and performing the experiment. I made the analysis for the experimental data, and contributed a minor part in writing the paper.

Paper III:
Inner-valence and core ionisation study of the fragmentation dynamics of 1,3-cyclohexadiene

V. Lindblom, S. Sahu, N. Walsh, M. Gisselbrecht, and S. L. Sorensen
In manuscript

I prepared and took part in the experiment. I analysed all the experimental data and wrote the manuscript.

Paper IV:
Dynamics in Core Excited Cyclopropane

V. Lindblom, S. Oghbaiee, S. Ganguly, J. Laksman, B. Oostenrijk, E. P. Månsson, N. Walsh, M. Gisselbrecht, S. L. Sorensen
In manuscript

I took part in the experiment, made all the analysis of the experimental data and wrote the manuscript.

Paper V:
Identification of the Roaming Mechanism and the Formation of H_3^+ in Core Ionised Cyclopropane

V. Lindblom, S. Ganguly, N. Walsh, M. Gisselbrecht, and S. L. Sorensen
Phys. Chem. Chem. Phys. 2026, **28**, 7344-7351

I took part in the experiment, made all the analysis of the experimental data and wrote the paper.

Paper VI:
ICE - A Mobile Reaction Microscope end station for AMO science at MAX IV Laboratory

N. Walsh, **V. Lindblom**, S. Ganguly, B. Oostenrijk, M. Gisselbrecht, S. L. Sorensen, M. Tchaplyguine, S. Appelfeller, A. Generalov, G. Öhrwall, and A. Preobrajenski
In manuscript

I took part in some of the commissioning experiments, I analysed part of the experimental data, and took part in the writing.

Acknowledgements

I would like to address my greatest thanks to my main supervisor Stacey for giving me support during my work and the many scientific discussion. I also thank Mathieu and Noelle for being my two co-supervisor and particularly with the aid and discussions during beamtimes. Additionally, thanks to Antti for reviewing my thesis with only a short period of time and yet providing very helpful and constructive feedback.

Populärvetenskaplig sammanfattning

Hur naturliga fenomen fungerar på en fundamental nivå är en frågeställning som alltid varit central inom vetenskapen. Alla vetenskapliga applikationer som idag används för att tillverka allt från medicin till datorkomponenter bygger på att ha en väl förstådd fundamental grund. Detta arbete studerar molekyler för att vidare förståelsen kring deras kvantmekaniska natur. Detta åstadkoms genom att studera olika elektroniskt tillstånd, övergången mellan dem och den dynamik som kan ske i tillstånden.

Elektromagnetisk strålning kan ändra det elektroniska tillståndet i en molekyl genom att ge molekylen energi. Om energin som ges överensstämmer med skillnaden mellan begynnelse tillståndet och ett nytt exciterat tillstånd sker en resonansövergång. Om energin är högre än en viss gräns kommer molekylen i stället att joniseras. Synkrotronljuskällor specialiseras på att ge väldigt brilliant och preciserad elektromagnetisk strålning. I detta arbete används det för att studera olika kolbaserade molekyler när kolets kärnelektron exciteras till olika resonanstillstånd runt joniseringskanten. När en kärnelelektron exciteras bildas ett hål som molekylen kommer vilja fylla med en elektron, detta sker snabbt utav en av valenselektronerna. Molekylen är nu i ett mycket exciterat tillstånd och kommer behöva göra sig av med överskottsenergin. Det sker (i kolatomer) genom att en elektron emitteras i ett så kallat Auger-Meitner sönderfall, vilket lämnar molekylen i ett (eller dubbelt) joniserat tillstånd. Dynamik kan ske redan i det kärnexciterade tillståndet, men även i det joniserade tillståndet.

I detta arbeta studeras tre olika aspekter i molekyler med hjälp av synkrotronljus. För det första, elektroniska övergångar i metanbaserade joner. Det vill säga joner med en enda kolatom och olika mängder väteatomer. Nya övergångar som inte syns i de motsvarande neutrala molekylerna observeras. Märkbart resultat är att de elektroniska övergångar kartläggs för den exotiska jonen CH_5^+, denna jon är fluxionell, vilket betyder att strukturen på jonen ändras spontant och kontinuerligt mellan olika lägen. För det andra, studeras hur excitation av kolatomer med olika kemiska omgivning påverkar Auger-Meitner sönderfallet. För det tredje, studeras den atomära dynamiken efter kärnexcitation mer noggrant genom att mäta momenten på alla fragment av en cyklisk kolvätemolekyl, cyklopropan, efter att den gått i sönder på grund av den höga laddning som erhållits. Detta leder till att en väldigt svår mätt dynamik lyckas avbildas. Denna dynamik är när ett neutralt fragment emitteras från original molekylen, men fastnar i en elektronisk potential och börjar vandra kring den resterande molekylen. Till slut abstraherar vandraren ytterligare ett fragment och de två kvarstående kropparna dissocierar sedan. I fallet för cyklopropan är det en vätemolekyl H_2 som vandrar och abstraherar en proton vilket bildar den fascinerade jonen H_3^+, vilket är en av de vanligaste molekylära jonerna i universum och spelar en stor roll i astrokemi.

Popular science summary

How natural phenomena work at a fundamental level is a question that has always been central to science. All scientific applications that are used today to manufacture everything from medicine to computer components are based on a well-understood fundamental basis. This work studies molecules to better understand their quantum mechanical nature. This is achieved by studying different electronic states, the transitions between them, and the dynamics that can occur in these states.

Electromagnetic radiation can change the electronic state of a molecule by giving the molecule energy. If the given energy corresponds to the difference between the initial state and a new excited state, a resonance transition occurs. If the energy is higher than a certain limit, the molecule will instead be ionised. Synchrotron radiation sources specialise in providing very brilliant and precise electromagnetic radiation. In this work, such radiation is used to study various carbon-based molecules when the carbon's core electron is excited to different resonant states around the ionisation edge. When a core electron is excited, a hole is formed that the molecule will want to fill with an electron; this happens quickly by one of the valence electrons. The molecule is now in a very excited state and will need to get rid of the excess energy. This happens (in carbon atoms) by emitting an electron in a so-called Auger-Meitner decay, which leaves the molecule in a single (or doubly) ionised state. Dynamics can already occur in the core excited state, but also in the ionised state.

In this work, three different aspects of molecules are studied with the help of synchrotron radiation. Firstly, electronic transitions in methane-based ions. That is, ions with a single carbon atom and different amounts of hydrogen atoms. New transitions are observed that are not seen in the corresponding neutral molecule. Notable results are that electronic transitions are mapped for the exotic ion CH_5^+, this ion is fluxional, which means that the structure of the ion changes spontaneously and continuously between different states. Second, we study how excitation of carbon atoms with different chemical environments affects Auger-Meitner decay. Third, we study the atomic dynamics after core excitation more carefully by measuring the momenta of all fragments of a cyclic hydrocarbon molecule, cyclopropane, after it has broken down due to the high charge that has been obtained. This allows a very difficult dynamic to measure to be successfully depicted. This dynamic is when a neutral fragment is emitted from the original molecule but gets stuck in an electronic potential and starts to roam around the parent molecule. The roaming fragment eventually abstracts another fragment from the parent molecule, and the two remaining bodies then dissociate. In the case of cyclopropane, it is a hydrogen molecule H_2 that roam and abstracts a proton, forming the fascinated H_3^+ ion, which is one of the most common molecular ions in the universe and plays a major role in astrochemistry.

Spectroscopy of core-excited molecules and exploration of the induced dynamics

Chapter 1

Introduction

Interactions of light and molecules create a plethora of processes, many of which induce dynamics, isomers through nuclei rearrangement, fragmentation through dissociation, or both. These dynamics are key to many biological and chemical processes which occur in nature, on earth and in space, in the human body, and in industrial or medical applications. This makes having knowledge on how the dynamics naturally occurs very important, that knowledge can then provide the ability to control the dynamics in a desirable way, creating necessary chemical products or destroying harmful pathogens or tumours in the human body.

The dynamics of the nuclei of molecules is caused by the electron configuration, which electronic states are occupied, and their character. Changing the electron configuration therefore allows for the study of the dynamics. In this thesis the different states and the changes they incur are investigated.

The transitions between states in molecules and atoms can be initiated by various means. Photons provide an easy access to the possible states of molecules and atoms, especially with synchrotron radiation from storage rings. These facilities now provide a wide range of precise energies, enabling great accuracy in experiments. Therefore, the states and transitions in this thesis are studied using synchrotron radiation, specifically in the soft x-ray regime where the carbon core excitations lay.

This thesis aims to explain the electronic state transitions in core-excited ions, site-selectivity of Auger-Meitner decay and dissociation mechanisms after core excitation/ionisation and the subsequent Auger-Meitner decay. The basic theory and underlying physics of these concepts will be shown in Chapter 2. To experimentally investigate the aforementioned concepts, we conducted the experiments at a storage ring and utilised synchrotron radiation. Chapter 3 outlines this radiation source and

each experimental instrument used. The results of the studies will be shown and discussed in Chapter 4. Chapter 5 will lastly summarise and provide an outlook of the work that was done and how it may be expanded upon.

Chapter 2

Theoretical background

The thesis studies electronic states, transitions between states facilitated by interaction with electromagnetic radiation, and the nuclear and charge dynamics that occurs after such transitions. This chapter introduces some of the key theoretical concepts and models that are fundamental for these studies.

2.1 Photons and molecules

The building blocks of molecules are the atoms, consisting of a nucleus and the surrounding electrons, bound by the attractive Coulomb force. In 1913 Niels Bohr put together a model of the atom [1], see Figure 2.1. It shows the nucleus as a positive mass in the centre, while the electrons orbit like planets around a star. The electrons are not allowed to do whatever they want; instead, they are locked to the orbitals (derivative from the word *orbit*). The orbitals are mathematically described by a wavefunction Ψ, and governed by the so called wave equation

$$\mathscr{H}\Psi(\bar{r},t) = i\hbar\frac{\partial}{\partial t}\Psi(\bar{r},t) \tag{2.1}$$

developed by Erwin Schrödinger [2]. The hamiltonian $\mathscr{H}$ is an operator that represent the total energy of a physical system. For example, the Hamiltonian of one particle can be written as

$$\mathscr{H} = -\frac{\hbar^2}{2m}\nabla^2 + V(\bar{r}), \tag{2.2}$$

where the first term is associated with the kinetic energy and the second term the potential energy. Even so, only the Schrödinger equation for the hydrogen atom

can be solved analytically, while larger systems can be solved numerically, or through the mean-field approximation where each electron is treated like a hydrogen electron combined with a field created by all the other electrons. Thus, the atomic orbitals can be expressed by hydrogen-like orbitals, as is explored further in section 2.3.

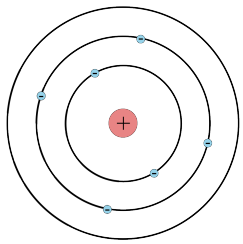

Figure 2.1: A schematic of the Bohr model of an atom, the sizes and distances are not to scale. The nuclei is the red dot in the centre and the electrons are shown as blue dots on the orbital paths in black.

Molecular orbitals can be illustrated by using Linear Combination of Atomic Orbitals (LCAO), where the wavefunctions of each atom are combined as

$$\Psi = \sum_i c_i \psi_i. \tag{2.3}$$

The coefficients c_i of all atomic wavefunctions ψ_i are summed together. Figure 2.2 shows how the atomic wave functions of two hydrogens build up in the hydrogen molecule. The two atomic orbitals form two molecular orbitals, if the two atomic orbitals are in phase they constructively interfere and overlap, while if they are out of phase they destructively interfere and form nodes. Bonding occurs when the wavefunctions overlap, resulting in a higher probability of finding an electron between nuclei. This lowers the energy of the state, causing them to bond. When nodes form in-between the nuclei, the energy will increase and the state is anti-bonding.

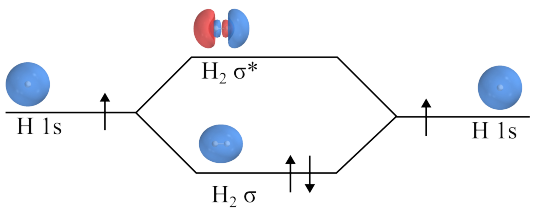

Figure 2.2: The linear combination of hydrogen atomic orbitals forming the molecular orbitals of H_2. The two electron (one from each atom), shown as arrows, are placed in the lowest energy orbital the bonding σ, while the anti-bonding σ^* remains empty.

2.2 Light and matter interactions

The interaction between photons and matter allows the study of the electronic structure of matter and in some cases controls its dynamics. The photoelectric effect [3] provides a relation between the photon and emitted electron of matter in

$$E_b = h\nu - E_k + \phi \tag{2.4}$$

where E_b is the binding energy and E_k is the kinetic energy. The ϕ is the work function which is mostly relevant when working with condensed matter, in gas phase molecules covered by this thesis the work function is zero.

Figure 2.3(a) shows how a core electron is ionised in the photoelectric effect. After photoionisation an atom or molecule is in an ionised state, the core-hole will be filled by another valence electron to relax the system. The energy difference between the core and valence state is released as kinetic energy to the electron. This emission can occur via a photon in florescence decay or by a second valence electron emission in a normal Auger-Meitner decay [4, 5], shown in Figure 2.3(b).

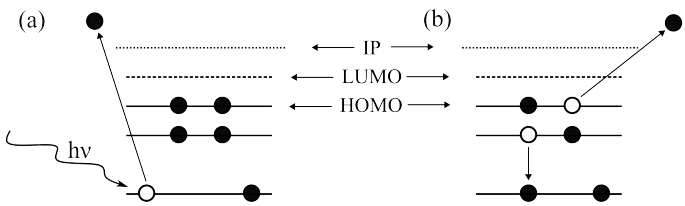

Figure 2.3: (a) Ionisation of a core electron by a photon with energy hν, and (b) normal Auger-Meitner decay after core ionisation. The highest occupied molecular orbit (HOMO), lowest unoccupied molecular orbit (LUMO), and the ionisation potential (IP) are highlighted.

The photoelectric effect describes the ionisation of matter, but if the photon energy is equal to the difference between two states it may excite an electron from the first state to the second. Figure 2.4(a) schematically shows this x-ray absorption. The probability for a transition from an initial state $|\psi_i\rangle$ to a final state $|\psi_f\rangle$ can be described by

$$P_{i\to f} = \frac{2\pi}{\hbar} \left|\langle\psi_f \left|\bar{\mu}\right| \psi_i\rangle\right|^2 \delta(E_f - E_i - h\nu) \tag{2.5}$$

where $\bar{\mu}$ is the dipole operator, and the δ is a Dirac-delta function imposing energy conservation. This expression is Fermi's golden rule. This dipole operator is introduced as an approximation of the interacting Hamiltonian, with $\mathscr{H}_{interaction} = -\bar{\varepsilon} \cdot \bar{\mu}$ where $\bar{\varepsilon}$ is the polarisation vector. As with ionisation of a core electron, the core hole will be filled by a valence electron causing an Auger-Meitner decay. Two possible pathways of the decay exists shown in Figure 2.4(b-c), (b) the excess energy

causes the original core electron to be emitted in a participator Auger-Meitner decay, (c) the excess energy causes a second valence electron to be emitted called spectator Auger-Meitner decay.

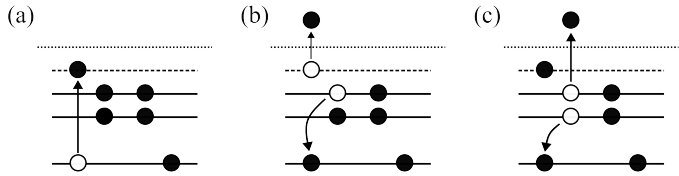

Figure 2.4: (a) Excitation of a core electron by a photon with energy hν. The system will decay by filling the core hole with a another valence electron, the excess energy will cause either (b) the excited electron to be emitted in a participator Auger-Meitner decay or (c) a second valence electron will be emitted in a spectator Auger-Meitner decay.

2.2.1 Molecular dynamics

Dications or ions with higher positive charge will generally cause dissociation in a short time scale because of the large repulsive Coulomb force, in what is commonly called a Coulomb explosion. The dissociation may occur in a single step, but in a three-body fragmentation or more it is common to have it occur in sequential steps. If a three-body fragmentation occurs in a single step, it is called a $concerted$ break-up while if it occurs in two steps it is called $sequential$. The concerted fragmentation of an dication (ABC^{2+}) will occur as

$$\begin{aligned} ABC + h\nu \rightarrow ABC^{2+} + e^-_{photon} + e^-_{auger} \\ \rightarrow A^+ + B^+ + C + e^-_{photon} + e^-_{auger} + KER \end{aligned} \tag{2.6}$$

where KER is the kinetic energy release in dissociation. The sequential break-up goes as

$$\begin{aligned} ABC + h\nu \rightarrow ABC^{2+} + e^-_{photon} + e^-_{auger} \\ \rightarrow AB^{2+} + C + e^-_{photon} + e^-_{auger} + KER_1 \\ \rightarrow A^+ + B^+ + C + e^-_{photon} + e^-_{auger} + KER_1 + KER_2 \end{aligned} \tag{2.7}$$

where the reaction ends up with two KER distributions. The fragment C will in this case have a constant fraction of the KER in the first step. Since the AB breakup does not affect C, no correlation is expected between C and either of A or B. Moreover, the AB breakup should in general produce opposite momentum vectors that are added to their initial momentum gained in the first step.

Molecular dissociation in neutral molecules from a chemical point of view is generally described in two ways. The first dissociation leads to closed-shell products by

traversing a large energy barrier, which consists of a transition state. The second leads to radicals from bond-breaks without potential barriers. In the early 2000s a third dissociation mechanism, called roaming, was experimentally shown by Townsend *et al.* in formaldehyde [6]. This dissociation occurs by first emitting a neutral fragment, which becomes trapped in a shallow potential energy surface. The neutral moiety roams around the parent molecule, until it eventually abstracts another part, leading to a dissociation [7]. This was shown to produced the closed-shell products of H_2 and CO from formaldehyde without entering the transition state and crossing an energy barrier that is normally required for those products. Figure 2.5 schematically shows the difference between the roaming moiety getting caught or not. The roaming mechanism has since then been found in several molecules and dications and is suggested to be ubiquitous [8–18]. It is difficult to observe directly and several approaches have emerged. **Paper V** explores the roaming mechanism in cyclopropane, leading to formation of the H_3^+ ion. Our method is to use momentum imaging of the fragmentation channel where the neutral have not yet abstracted the second part from the parent, providing insight during the roaming process.

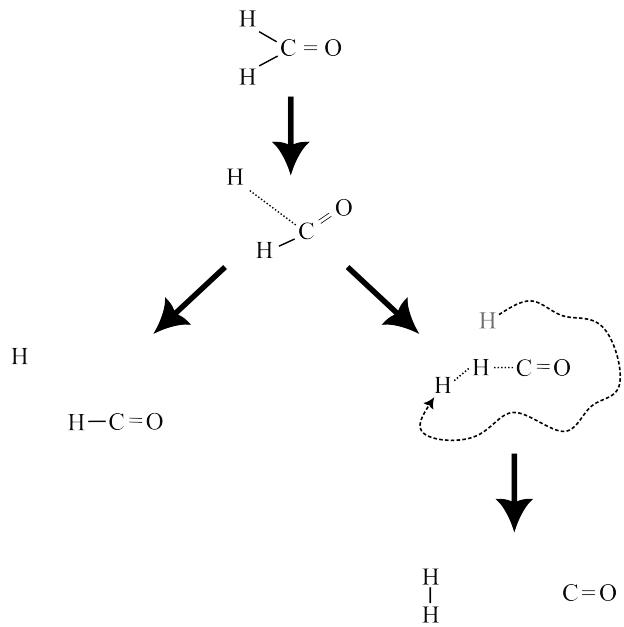

Figure 2.5: Schematic of formaldehyde dissociation. One hydrogen gets emitted by a bond elongation, on the left the bond breaks and the hydrogen is lost. While on the right, the hydrogen gets trapped by a potential energy surface and starts roaming around the parent. The roaming hydrogen then abstracts the second hydrogen and dissociates.

2.3 Molecular quantum chemical calculations

For most quantum chemical calculations in this thesis the software package OpenMolcas [19–21] was used. In this section the main programs and basis sets that were utilised will be briefly presented.

The initial setup for a calculation requires selection of a basis set and (initial) geometry of the atom or molecule. In general the ANO-RCC-VQZP basis set was used, this is an Atomic Neutral Orbital (ANO) type bases set, with Relativistic Core-Correlated (RCC) and with Valence Quadruple Zeta accuracy with added polarisation functions (VQZP) [22]. The RCC component means that the basis set has been contracted using the Douglas-Kroll Hamiltonian [23, 24] to include relativistic effects in the quantum chemical calculation. When dealing with Rydberg states like in **Paper I** an auxiliary basis set is added. This additional basis set is a diffuse atomic like basis set contracted onto the molecular centre of charge.

The one-electron wave function is then created using self-consistent field method (SCF), however, for the systems studied in this thesis a Multi Configurational (MC) method is then applied to take electron correlation into account. This is done through the RASSCF [25–27] program where the orbitals are grouped into three different active spaces: RAS1, RAS2, and RAS3. These three spaces have different interactions, RAS1 can be set to allow a certain number of holes, while RAS3 can be set to include a set of allowed electrons. RAS2 allows all possible configurations and is therefore equivalent to a complete active space (CASSCF) calculations when used on its own. The main benefit of these three spaces is that one can easily designate which orbitals should have a hole and which should become occupied by an electron. The wave-function energy calculation is usually improved by adding some perturbation theory through RASPT2 [28, 29], this is an computationally expensive method.

When doing geometry optimisation the program SLAPAF is used, this program perturbs the initial geometry and is put into a minimisation loop [30]. By recalculating the ground state (or excited state if specified) energy in each minimisation loop, the program eventually finds the lowest energy geometry of the molecule. It should be noted that the minimization can end up in a local minimum, but in general this is a very effective way of finding theoretical structures of unknown samples.

Once the wave-function is computed and the geometry is defined Fermi's golden rule can provide the transition probability between two different states. This is accomplished through the RASSI program [31, 32], with the wave-function for the states involved in the transition as inputs. Many different variables can result from this program, however, in this thesis it was mainly used to calculate the oscillator strength from a ground state to core excited state. The core-excited states were optimized by

imposing core-valence separation in order to avoid variational collapse due to filling the core orbital. In this thesis this was done through the use of the HEXS method [33].

Chapter 3

Instrumentation

The previous section introduced many of the key concepts that were studied in this thesis, while this chapter aims to explain the various methods used to study them and motivate why they were chosen. The study of molecular (or ion) dynamics is a very broad subject and many different types of methods have been developed. This includes both what is used to initiate the process, and how it is measured. One of the most common ways to initiate dynamics is through electromagnetic radiation. For this thesis the source of the electromagnetic radiation was storage rings, which provide synchrotron radiation as explained in the next section. Moreover, this chapter will cover the various experimental setups which were used to capture and measure the particles and consequently the dynamics. These range from simple time-of-flight (TOF) detectors to complicated 3D momentum imaging in coincidence spectrometers.

3.1 Synchrotron radiation

Higher energy photons (in the X-ray range) were first discovered by William Röntgen [34], using a high-voltage discharge tube. This way of creating light, called *bremsstrahlung*, requires charged particles to be accelerated to several kV. One way to achieve these high speed particles is to have the particle pass a single radio-frequency cavity several times by going around larger and larger circular tracks. But, when the charged particles follow a curved path it emits radiation, synchrotron radiation. The emission of electric fields from a moving charge is described by [35, 36]

$$E(x,t) = \frac{e}{4\pi\epsilon_0}\left[\frac{\bar{n}-\bar{\beta}}{\gamma^2(1-\bar{\beta}\cdot\bar{n})^3R^2} + \frac{1}{c}\frac{\bar{n}\times[(\bar{n}-\bar{\beta})\times\bar{\beta}]}{(1-\bar{\beta}\cdot\bar{n})^3R}\right]. \qquad (3.1)$$

The $\bar{n}$ is the unit vector from the particle to the observer, R is the distance from the point of radiation emission to the observer, e the electric charge, ϵ_0 the capacitivity of free space, γ the Lorentz factor, c is the speed of light and $\bar{\beta} = \frac{\bar{v}}{c}$, where $\bar{v}$ is the electron velocity. The second term describes the far (acceleration) field and the produced synchrotron radiation when perpendicular to the velocity, $\bar{\beta}$. This was first viewed as a disadvantage as energy was lost from the particles, but use of the radiation was quickly found. The 1st generation synchrotron radiation facilities used this radiation parasitically from high energy physics experimental facilities.

Dedicated facilities were then created to produce synchrotron radiation and use it to study light-matter interactions. The 2nd generation synchrotron radiation sources used the same method as previous, bending magnets, to produce the light. The 3rd generation synchrotron radiation sources produces the radiation through insertion devices (arrays of magnets). The current new generation (4th) produces the most brilliant light and is defined by being diffraction limited (i.e. the emittance of the electron beam is comparable with the size of the x-ray beam). The insertion devices work by having the relativistic electrons oscillate when travelling through the magnet array as shown in Figure 3.1, where an undulator is shown. The undulator produces coherent light with a wavelength of

$$\lambda_i = \frac{\lambda_u}{2\gamma^2 i}(1 + \frac{K^2}{2} + \frac{\theta^2\gamma^2}{2}) \tag{3.2}$$

where λ_u is the period length of the undulator, θ is the angle between the electron velocity and the radiation direction, and $K = \frac{eB\lambda_u}{2\pi m_e c}$ is an undulator parameter where B is the peak magnetic field of the magnets in the array and m_e is the mass of the electron. The radiation produced from an undulator is coherent, although another insertion device called the "wiggler" functions as a wavelength shifter. The benefits depend on the experiment that uses them; in this work, only undulators were used.

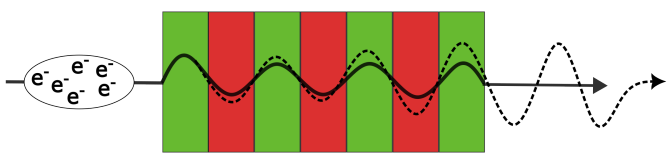

Figure 3.1: A schematic of the principle of an undulator. The undulator consists of an array of magnets with periodically opposite polarisation. The electron bunch travels through the undulator on a sinusoidal path due to the alternating B-field. The bending acceleration of the electrons causes photon emission with polarisation in the same plane as the acceleration, depicted as dashed arrow. If the electrons are travelling at relativistic speed, the photons will primarily be emitted in the forward direction.

In a synchrotron light source, electrons circulate in a storage ring. The general setup of a storage ring is shown in Figure 3.2. In essence, electrons are first accelerated to

near light speed by a linear accelerator, LINAC, then they are injected into the storage ring as bunches, where three main components are found. Firstly, the undulator as described before. Secondly, the radio-frequency cavities (RF-cavity) accelerate the electrons, as they slowly lose speed in the ring due to radiation or collisions. These RF-cavities also aid in stabilising the electron bunches as the slower electrons are accelerated and the quicker electrons are retarded. This helps provide a stable current in the ring. The third component is the bending magnets, which keep the electron bunches going in a circle, storage rings also have magnets to focus bunches for stability and better light emitting conditions.

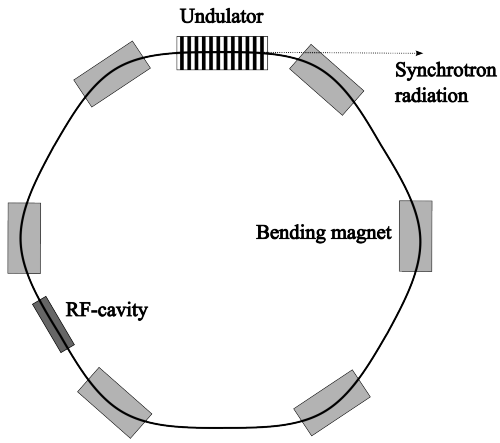

Figure 3.2: A schematic of a storage ring, with three of the major components: A bending magnet, RF-cavity and an undulator.

There are many storage rings around the world. The experiments in this thesis utilised two such facilities: MAX IV in Lund, Sweden and BESSY II in Berlin, Germany. MAX IV is a fourth generation synchrotron facility with two storage rings, one with 1.5 GeV electron energy and one with 3 GeV, while BESSY II is a third generation synchrotron facility with one 1.7 GeV storage ring. Both of these facilities have many beamlines where experiments can be done, this thesis used three beamlines, whose parameters are listed in Table 3.1.

Table 3.1: The parameters for the beamlines where experiments were conducted as part of this thesis. Only linear polarised light was used, but FinEstBeAMS and UE52_PGM are able to use elliptically polarised light. This is indicated by their use of either linearly polarised undulator (LPU) or elliptically polarised undulator (EPU).

Beamline	Facility	Energy ranges	Radiation source	Focus spot size h x v
FlexPES [37]	MAX IV	$43 - 1550$ eV	LPU	50 x 15 μm
FinEstBeAMS [38]	MAX IV	$4.5 - 1300$ eV	EPU	100 x 100 μm
UE52_PGM [39]	BESSY II	$120 - 160$o eV	EPU	600 x 700 μm

After light is produced by the insertion devices the beamline exists to "shape" the light and house the experimental setups. A key component is the monochromator which is designed to extract a narrow wavelength window from the undulator spectrum. This is done through a dispersive element, like a diffraction grating, in combination with an exit slit which lets through a small part of the dispersed light. Another important component of the beamline is the mirrors which focus the light beam into a small spot where the experimental sample may be interacted with.

The benefit of the synchrotron radiation is firstly the variability of photon energy, produced by altering the B-field, see equation 3.2. This is practically done by moving the magnet arrays closer to (or further away from) each other. No other light source can produce the large range of photon energy. Secondly, together with the large photon energy range is that the selected light has in general a very small bandwidth compared with other sources. This is paramount when studying resonant processes. Another very important aspects is the coherence granted by the undulators, this attribute was however not utilised in this thesis.

3.2 Experimental setups

This section will describe the four experimental setups used in this thesis. Firstly, with the ion trap and the mass spectrometer for ions used in **Paper I**. Secondly, the hemispherical electron analyser which was used for Auger-Meitner decay spectroscopy in **Paper II**. Thirdly, the combination of a hemispherical electron analyser and an ion mass TOF spectrometer used in **Paper III**. Lastly, a reaction microscope, ICE (Ions in Coincidence with Electrons) described in **Paper VI**, which measures both ions and electrons in coincidence, and specifically captures the 3D momentum of these particles which was employed in the dynamic investigations of **Paper IV-V**.

3.2.1 Ion trap

Free ions are in general difficult to study, requiring specialized equipment to successfully do so. One of the main reasons for this difficulty is that they are highly reactive. The ions are of course also charged, and repel each other making it challenging to achieve sufficient high density sample. However, due to this inherent charge it is possible to steer them by the use of electromagnetic fields which is impossible for neutral molecules. This control is the basic principle for ion traps. The combination of the ion trap with synchrotron radiation allows for XAS-like experiments. The benefit of looking at the ion is that new states can emerge or be suppressed due to selection rules, allowing exploration of new electric potential energy surfaces and the dynamics they

may impose. Another key benefit is in general access to species not found naturally, readily or exotic species such as CH_5^+.

The ion trap used in this thesis was the Nanocluster Trap end-station [40] which is located at the UE52-PGM beamline [39] at BESSY II in Berlin, Germany. This setup was used for the experiments presented in **Papers I**. Figure 3.3 shows a schematic of the end-station, and will be described in the following three parts: production, trapping, and detection.

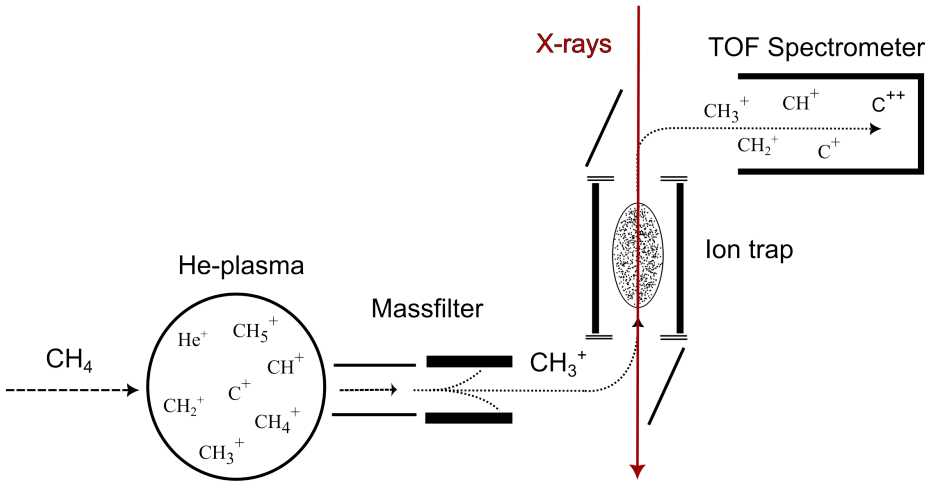

Figure 3.3: A schematic of the whole process from neutral particle to detected mass fragment for the case of methane. At the left side the sample molecule, methane, is introduced to a highly energetic He-plasma and all ionic species are formed. The ion of interest is filtered by the electromagnetic filter (CH_3^+ with a m/q of 15 in the schematic), and guided into the ion trap. The content of the trap interacts with the X-rays and periodically a sample of the content is let out of the end-cap. This sample is guided to a reflectron TOF mass spectrometer, that provides a measurement of the m/q spectrum of the contents of the ion trap.

Production

The sample gas is introduced into a highly energetic helium plasma produced by a magnetron sputtering source. The molecules are ionised and possibly fragmented, this produces a soup of helium and ions from the sample. The ions are then extracted and guided by a radio frequency hexapole into a radio frequency quadrupole mass filter. The ion to be investigated is filtered by a small range of mass-to-charge ratio and passes on towards the ion trap. Entering the trap a helium buffer gas is introduced to cool the ions, ensuring that they are primarily in the ground state.

Trapping

Figure 3.4 shows a schematic of the cryogenically cooled quadrupole ion trap [41]. In essence the trap consists of four closely spaced alternately charged rods and two end-caps. The voltage of the rods alternates polarity pairwise and traps the ions radially. The end caps have high potentials and traps the ions in the axial direction. The trapping is based on the principles of the Paul trap [42].

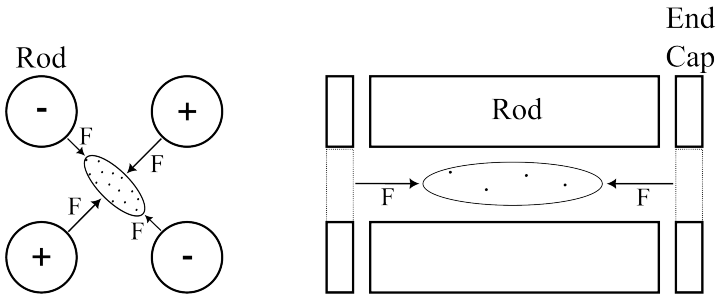

Figure 3.4: The ion trap is made up of four charged rods, with alternating charge (pairwise). The end-caps are also charged, completely trapping the charged ions. This creates trapping forces conceptually shown by F.

The synchrotron radiation is delivered in the axial direction of the trap, and is not a focused beam but instead a low divergent beam. This is done to have the radiation interact with ions throughout the trap rather than at a single point. The beamline can deliver photons in the range of $85 - 1600$ eV with a resolving power $E/\Delta E$ of more than 10000 at 400 eV and variable polarisation, though only horizontal linear polarisation was used in the experiment presented in this thesis.

When a sample ion absorbs an X-ray photon, an inner-shell electron is excited or ionised, Auger-Meitner decay follows and the ion may fragment into smaller charged species. All resulting ions are accumulated in the trap. The exit end-cap is periodically switched off (usually at a rate of $1 - 200$ Hz) letting out a sample of the current mass fragment composition. The ion trap is meanwhile being continuously refilled with ions.

Detection

The ions which are pulsed out of the exit end-cap are guided towards a time-of-flight (TOF) mass spectrometer of a reflectron type, schematically shown in Figure 3.5. The ions are first accelerated, then allowed to separate in a drift tube, and the separation occurs due to the different speeds obtained by ions having different mass-to-charge

ratios. Lastly, the ions are reflected onto a detector which records the time. The recorded TOF is converted into mass over charge ratio by

$$TOF \propto \sqrt{\frac{m}{q}}, \tag{3.3}$$

where m is the mass and q the charge of the detected particle. This allows identification of what fragments are in the trap, creating mass spectra from the data.

The measurement procedure is to scan the photon energy over some range, while the mass spectra are recorded at each energy step for some specified time, producing a map shown in Figure 3.6(a). One mass fragment can then be chosen, and is integrated over the mass bins it spans. Figure 3.6(b) shows the partial ion yield spectrum of the chosen fragment. This provides information on how the photon energy influences the probabilities of different means of decay, and the achieved spectra can be considered proportional to a X-ray Absorption spectrum (XAS) [43].

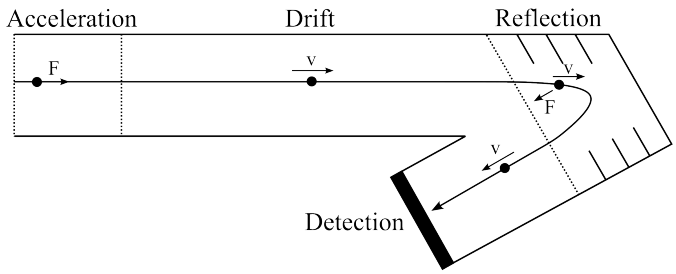

Figure 3.5: A schematic of a reflectron TOF mass spectrometer. The particle (ion) is first accelerated such that the initial velocity can be neglected. Then the particles are separated in time by their m/q in the drift region, then lastly they are reflected onto a detector.

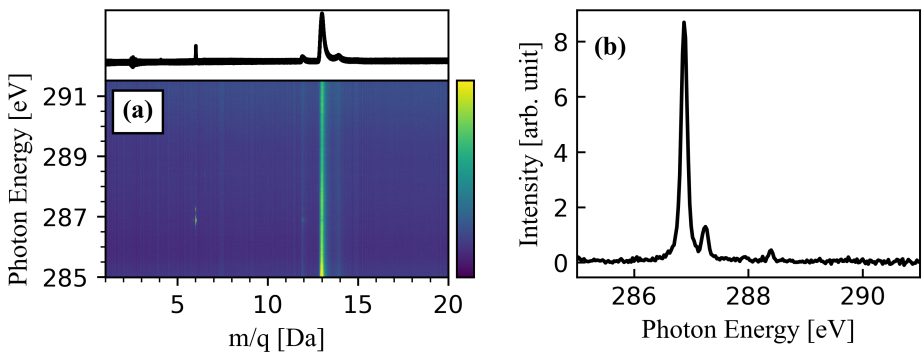

Figure 3.6: (a) A 2D mass spectra of CH^+ with time of flight equivalent mass bins on the x-axis and photon energy on the y-axis. An integrated spectrum of the mass bins is shown on top. (b) A partial ion yield of CH^+ from integrating the C^{2+} mass peak and plotting it against the photon energy.

The measured spectra may contain noise or background, in the form of for example dark counts. This is accounted for by obtaining a data point, or mass spectrum, without light. This is automatically done after each measurement, as the background level can shift from measurement to measurement but also due to external factors. The background is then removed by

$$difference = \frac{measurement - background}{photocurrent} \tag{3.4}$$

which gives the resulting spectrum denoted as $difference$. This subtraction is schematically shown in Figure 3.7, in this calibration the photocurrent is also taken into account, measured with a photodiode.

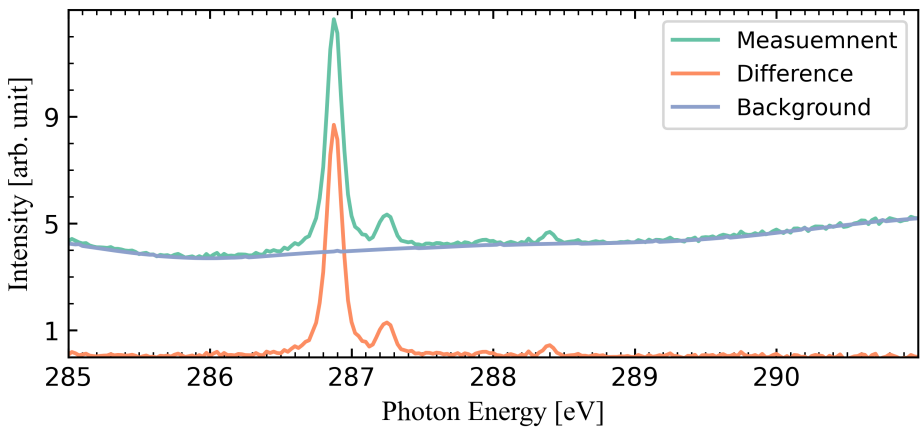

Figure 3.7: A depiction of how the background is subtracted from the total ion yield spectra from the ion traps works. The background (solid blue) is subtracted from the measurement (solid green) providing the useful ion yield spectrum (solid orange). The photocurrent has been accounted for in all lines.

3.2.2 Hemispherical electron analyser

The key attributes of electrons that make them easier to measure than most other particles, is that they are charged by q=-e and have an exact mass of m_e=5.4858e−4 amu. This means that under the influence of an electric field their path is simple to calculate by the Lorentz equation

$$\bar{F} = q(\bar{E} + \bar{v} \times \bar{B}), \tag{3.5}$$

where q is the charge, $\bar{v}$ the velocity vector, $\bar{E}$ and $\bar{B}$ the electric and the magnetic field-vectors. The hemispherical electron analyser uses this by having an applied electric field between two hemispheres as depicted in Figure 3.8. Electrons that enter the

hemisphere follow a curved path and electrons of a selected energy will reach the detector. If the energy of the electron is too high or too low the electrons will hit the walls and not be detected. The energy needed for the electrons to reach the detector is called the pass energy, and is directly related to the applied electric fields. The detector has a multi channel anode and thus the energy of detected electrons will have some dispersion from the pass energy. A higher pass energy will in general cause a higher dispersion of electrons to hit the detector, lowering resolution but increasing transmission and vice versa for a lower pass energy. The benefit of an hemispherical electron analyser is that one can collect a wide range of electron energies with high resolution. They are, dependent on the applied lens and static electric fields, capable of detecting photoelectrons and Auger-Meitner electrons with hundreds of eV kinetic energy.

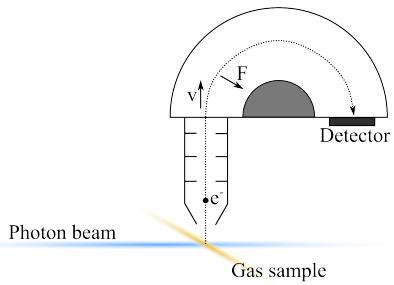

Figure 3.8: Schematic of a generic hemispherical electron analyser. An electron is emitted from a photon-molecule interaction, and is accelerated by lenses into the hemisphere. The two hemispheres are electrically charged causing a radial (inward facing) force on the electron, which gain follows a curved path. If the electron has the correct energy i.e. the pass energy, it reaches the detector.

The hemispherical analyser (Scienta R4000) used in this thesis on its own was initially situated at the I411 beamline of the MAX Laboratory, Lund, Sweden [44]. However is now situated at the FlexPES beamline at MAX IV [37]. The analyser can use many different sample solutions, in this thesis only a gas cell was used. This allows for a continues flow of sample gas at a stable pressure. The entire spectrometer is able to rotate to measure at different angles of emission, this is important as the light is horizontally polarised and thus the emission is angle dependent. However, in this thesis the angular distribution of electron emission was not studied using this spectrometer and thus it was kept at the "magic angle" of $54.7°$ in relation to the polarisation vector. This means that the intensity of electron emissions from orbitals of different character are independent of the angle of emission. When the electrons enter the spectrometer they first encounter a set of electromagnetic lenses which focus but also change the velocity by either acceleration or retardation. This allows the user to study different electron energies while keeping the pass energy (and therefore the resolution) constant. The detector is made up of a Multi-Channel Plate (MCP)[45] to amplify the electron signal and a Charge Coupled Device (CCD) camera to register a hit.

3.2.3 Electron-ion coincidence spectrometer

Capturing electrons in coincidence with ions from a single ionisation event allows for precise studies of the molecular dynamics associated with specific electronic states. The coincidence spectroscopy technique was first introduced by Eland *et al.* [46], but has since evolved into many different types of setups. This and the next section will cover two different types.

The first type of coincidence spectrometers discussed here is situated on the GPES endstation [47] at the FinEstBeAMS beamline [38] at MAX IV, in Lund, Sweden. The coincidence chamber consists of a hemispherical electron analyser (Scienta R4000 from Scienta Omicron) and a momentum-resolving ion TOF spectrometer. Furthermore, the inner part of the chamber is clad with μ-metal to shield from external magnetic fields. The ion part was only used as a TOF spectrometer in this thesis. The coincidence is set up to work with a pulsed extraction for the ions. When an electron is detected in a kinetic energy window of interest a trigger initiates an extraction pulse, accelerating ions towards the TOF spectrometer. This electron hit is also used as t_0 for the ion TOF. A needle effusive jet is generally used in order to increase the pressure in the interaction region.

The Scienta R4000 electron spectrometer is almost identical to the spectrometer described in Section 3.2.2 but has been modified to, instead of a MCP and CCD camera, have a three-plate MCP (Z-stack configuration) and a fast resistive anode position-sensitive detector [47]. This simplifies the coupling between electron and ion hits in events based measurements. In other words it allows each electron hit to be given an exact analogue XY-position signal.

The ion TOF spectrometer is a modified Wiley-McLaren type TOF analyser [48], but it is modified to have two electrostatic lenses, instead of homogenous electric fields determined by grids. This modification allows the setup to be optimised for momentum imaging or TOF resolution by adhering to the Wiley-McLaren conditions. This is because when the Wiley-McLaren conditions are fulfilled the TOF only depends on the m/q ratio of the ion, no momentum distribution along the spectrometer axis is possible. Therefore, the optimisation for momentum imaging means that the TOF peaks are spread out to provide momentum along the spectrometer axis, but this introduces asymmetry dependent on the angular emission of the particle due to the electric fields, which must be corrected for afterwards. The detector consists of an MCP pair together with a HEX-anode delay-line scheme[49, 50], allowing multi-hit events (as long as they differ in time or position) to be efficiently detected with zero dead-time [51, 52]. Dead-time refers to saturation of the detector at a single point, causing multiple hits to register as one, losing information.

This spectrometer setup allows studies of the ion fragmentation in coincidence with electrons from specific states. In this thesis, Auger-Meitner electrons after resonant excitation around the C 1s threshold were measured in coincidence with ions. Providing fragmentation information at final electronic state configurations.

3.2.4 3D momentum electron and ion imaging spectrometer

The last experimental setup is a versatile REaction MIcroscope (REMI), situated at the FlexPES beamline[37] at MAX IV. The ICE (Ions in Coincidence with Electrons) spectrometer was commissioned and is thoroughly described in **Paper VI**. A reaction microscope enables measurements of the 3D momentum distribution of electrons and ions in coincidence from a photo-reaction event. Furthermore, a 4π collection efficiency is attainable allowing the full kinematics to be determined from molecular dissociation processes. The spectrometer can be run in two modes, a lens mode and a RIMS (recoil ion momentum spectroscopy) mode.

The spectrometer consists of 150 copper electrode plates with circular holes. These plates are stacked 5 mm apart and are initially connected via 1 MΩ resistors, although the lens mode has other connections to create the electromagnetic lensing and will be discussed later. Figure 3.9(a) shows a schematic of the lens mode connections, and Figure 3.9(b) shows a picture of the spectrometer inside the vacuum chamber. The spectrometer is kept under high vacuum (10^{-8} mbar) during use. This spectrometer accelerates particles by static electric field after they are ionised by the synchrotron radiation. On each end of the spectrometer a detector, made up of a MCP and HEX delay-line anode, is situated and provides position XY and stop time for the TOF. The start time for the TOF is given by a bunch marker provided from the storage ring. This means that XYT coordinates are provided for both the electrons and ions. A coincident event is initiated by an electron hit, as the electron travels much faster than ions. This should in general be the photoelectron, as any potential Auger-Meitner electron would have too much energy (hundreds of eV) to be confined by the fields of this spectrometer. After the event starts, all the ions and additional electrons detected within a time window are assigned as part of that event. Then after the end of the time window a new event will start with the next electron hit. The size of the window is a changeable parameter, usually around 30000 ns.

With the XYT-coordinates the momentum vector $\bar{p}$ can be calculated for each particle by the following three equations

$$p_x = m\frac{x}{TOF}, \tag{3.6}$$

$$p_y = m\frac{y}{TOF}, \tag{3.7}$$

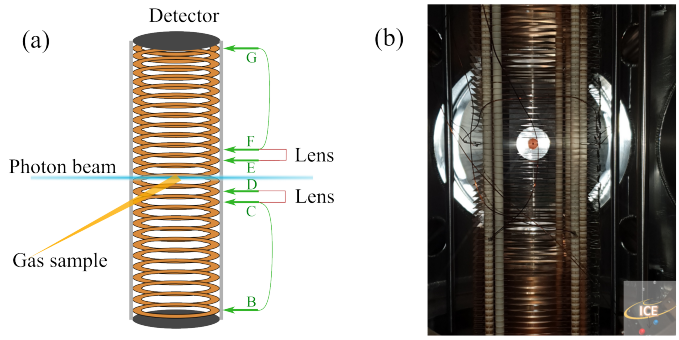

Figure 3.9: (a) A schematic of the ICE spectrometer, with the lens mode electrodes marked. The photon beam is schematically shown to interact with the gas jet in-between the two electromagnetic lenses. (b) A photograph of the spectrometer showing the stacked plates and support structure (rods). The source inlet (skimmer) is located in the middle and made out of copper.

and

$$p_z = qE \cdot \Delta TOF. \tag{3.8}$$

Where E is the applied electric field, and ΔTOF is the difference between the actual measured TOF and the nominal TOF of that particle if it had no momentum in the z-axis (spectrometer axis). The kinetic energy of each particle is:

$$KE = \frac{|\bar{p}|^2}{m}, \tag{3.9}$$

knowing the KE of all particles of a single event in a coincidence measurement provides the kinetic energy release (KER) of the fragmentation.

The spectrometer chamber can be used with a variety of different sample sources, however, in this thesis only a molecular beam source was used. The beam is produced by differential pressure of the spectrometer chamber and sample chamber through two skimmers. Due to the vacuum expansion, the thermal motion of the particles is significantly reduced, and the molecules can thus be considered cold or in their ground state. This is also beneficial because the initial momentum due to thermal motion will be close to zero, and thus even lower than achieved by a needle. Another difference from a needle is that the sample target is small and can therefore be placed to perfectly align with the light focus, making the interaction region small. For a dispersed sample from a needle, the chamber will be 'filled' with the sample (the sample will have highest density around the actual needle point) and the light will interact along the entire spectrometer to some extent. The beam makes the sample have a very large initial momentum in the beam direction (usually perpendicular to the light).

An important aspect of momentum imaging while using a molecular beam is to compensate for the large initial momentum. Due to the initial velocity the momentum of the fragments depend on the mass as

$$p_x = p'_x + m \cdot v_{mb}(x) \tag{3.10}$$

where p'_x is the momentum in the x-direction in the molecular frame and v_{mb} is the beam velocity. Here it is assumed that the jet is in the x-direction. Furthermore the molecular velocity v_{mb} will affect fragment velocities differently dependent on the mass m. Figure 3.10 shows an example of how the mass position changes in the x-direction for different TOF. Obtained by fitting v_{mb} with

$$x = x_0 + v_{mb}(x) \cdot TOF \tag{3.11}$$

where x_0 is an offset of the interaction point (between the molecular jet and photon beam) and the centre of the detector. Using the x_0, an initial $p_{x,0}$ is obtained from equation 3.6, and then the final momentum is the difference $p_{x,f}$=p_x-$p_{x,0}$.

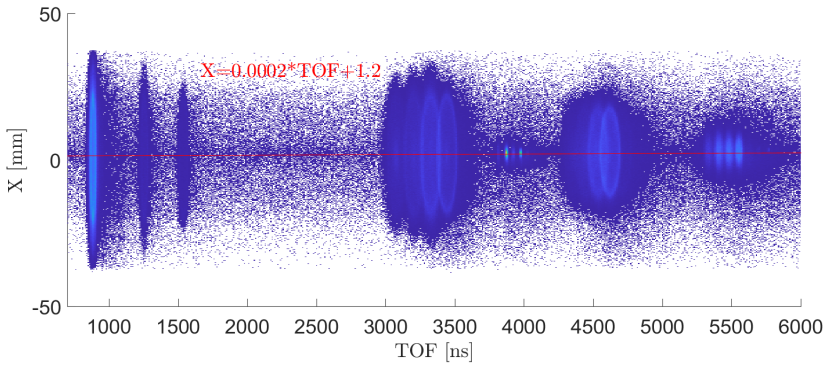

Figure 3.10: An example of the molecular jet used on the ICE spectrometer, here with the sample cyclopropane. The time of flight is plotted against the X-coordinate on the detector. Each ellipse represent a mass fragment, and each centre of these distribution is moving away from the x=0 with more mass. This provides a linear relation to calculate the velocity of the jet, in this case v_{mb}=0.0002 mm/ns.

Lens mode

The Lens mode is so named because is utilises lenses to accelerate and image the charged particles. This mode uses higher electric fields so that the electron TOF is below 10 ns. This is important because in the 1.5 GeV ring at MAX IV electron bunches are separated by 10 ns. Keeping the electron TOF lower than that reduces false coincidences. The high fields require lenses to disperse the image on the detector for higher resolution momentum imaging. The extraction field is created by a potential drop between electrode D-E (see Figure 3.9(a)), and the potential in the

interaction region is approximately 110 V/cm. The B-C and F-G electrodes are connected and thus placed at the same potential, creating drift regions. Electromagnetic lensing is obtained by imposing a high gradient between electrodes C-D and E-F.

RIMS mode

The RIMS mode is set up to run equivalently to Cold Target Recoil Ion Momentum Spectroscopy (COLTRIMS) spectrometer [53]. In this mode two opposite potentials are set just before the two detectors, creating a constant gradient in the E-field over the entire spectrometer. This field is lower than in the Lens mode, and therefore it can only be used when the storage ring is running in 'single-bunch' mode, where the times between each light pulse are 320 ns. The lower field would normally also mean that not all electrons are captured; introducing a magnetic field parallel to the spectrometer axis resolves this. This forces the electrons into a spiral path according to equation 3.5 and allows a 4π detection efficiency even for higher energy electrons (depending on the applied magnetic field strength). Ions are not affected by the magnetic field.

Chapter 4

Results and discussion

This chapter will provide summaries of the main results of the papers in this thesis. The main topics of the papers will be introduced, and the results will be shown and discussed. A lot of detail will be omitted in this chapter, and interested readers are referred to the individual papers. The focus of this thesis lies in spectroscopy, but it was also expanded into looking at isomerisation and fragmentation dynamics. This chapter will be split into three parts, section 4.1 is about the X-ray Absorption Spectroscopy (XAS) of ions, specifically the methane series CH_n^+ from **Paper I**. Section 4.2, looks at Auger-Meitner decay and how site-selectivity affects the propensity of this decay in two different molecules, ethyl trifluoroacetate (**Paper II**) and cyclohexadiene (**Paper III**). Lastly, section 4.3, will look at an investigation of the dynamics of cyclopropane. This includes both state-selective isomerisation (**Paper IV**) and a look at the roaming mechanism that leads to the formation of H_3^+ (**Paper V**), as well as a look at fragmentation pathways of the triply charged ion.

4.1 X-ray absorption spectroscopy on cations

The X-ray absorption spectra of ionic species is carried out by scattering soft x-rays on singly-charged ions using the ion trap, described in section 3.2.1. Measurements were taken from below the first core excited state to around the core double ionisation threshold. In XAS of a cation the selection rules are more restrictive than for XPS, and different electronic configurations exist in the core-excited ion which leads to new states emerging and suppression of other states when compared to the neutral XPS. Furthermore, multi-excited configurations can be populated in XAS leading to the observation of new states, as it was previously reported with the same technique for

N_2^+, O_2^+, CO^+, NO^+, and N_2H^+ [54–58].

4.1.1 Methane related ionic species, CH_n^+

The CH_n^+ series of ions are the smallest hydrocarbons, and appear in a large range of applications and studies. Theses range from basic organic chemistry all the way to astro- and plasma physics [59–62]. In the experimental setup the methane is introduces to the He plasma, creating all possible ions from C^+ all the way up to CH_5^+. We have measured spectra from all of them over the near threshold region as shown in Figure 4.1. Our measurements of C^+ and CH^+ compare well with published measurements [63–69], and show that the method and theoretical calculations work well. The CH_2^+ to CH_5^+ spectra have never been studied using XAS before. The resolution of the spectra differs primarily because of the instabilities of the cations, leading to low signal from some species. This is especially true for the two heavier cations, CH_4^+ and CH_5^+. This instability comes from their fluxional nature, which will be discussed later in this section. The highest quality spectrum is CH_3^+, and its assignment will therefore be covered in more detail in the following section.

Vibration and Rydberg states of CH_3^+

The XAS spectra can be split into two parts, the initial π^* excitation, which in the case of CH_3^+ shows a clear vibrational structure (Figure 4.2) and then the higher states, including satellite states and a distinct Rydberg series (Figure 4.3).

Figure 4.2 shows the 1s$\rightarrow\pi^*$ state and exhibits two vibrational modes, v_1 = 405 meV and v_2 = 45 meV, which are assigned to a CH stretch vibration and an umbrella-like vibration, respectively. This is similar to what has been observed in neutral CH_3 [70, 71], although the umbrella vibrational mode has higher energy in the ion. This is most likely due to the π^* being occupied by a single electron in the excited ion case, while fully occupied in the excited neutral. Another interesting aspect is that there is no evidence of symmetry break of the planar ion, with the exception of the umbrella vibration. There are degenerate π orbitals and thus the ion could change geometry to split these states, much like the pyramidal geometry observed in NH_3, but this does not appear to be the case in CH_3^+.

The higher energy states in Figure 4.3 start with a broad feature which is assigned to σ^* anti-bonding state, of a shape-resonant character. The shape resonance have a extremely short lifetime, and due to the Heisenberg uncertainty principle the uncertainty in energy is therefore large [72], providing a broad feature in the spectra, but this is not reflected in the theoretical calculations. Then a clear Rydberg np transition

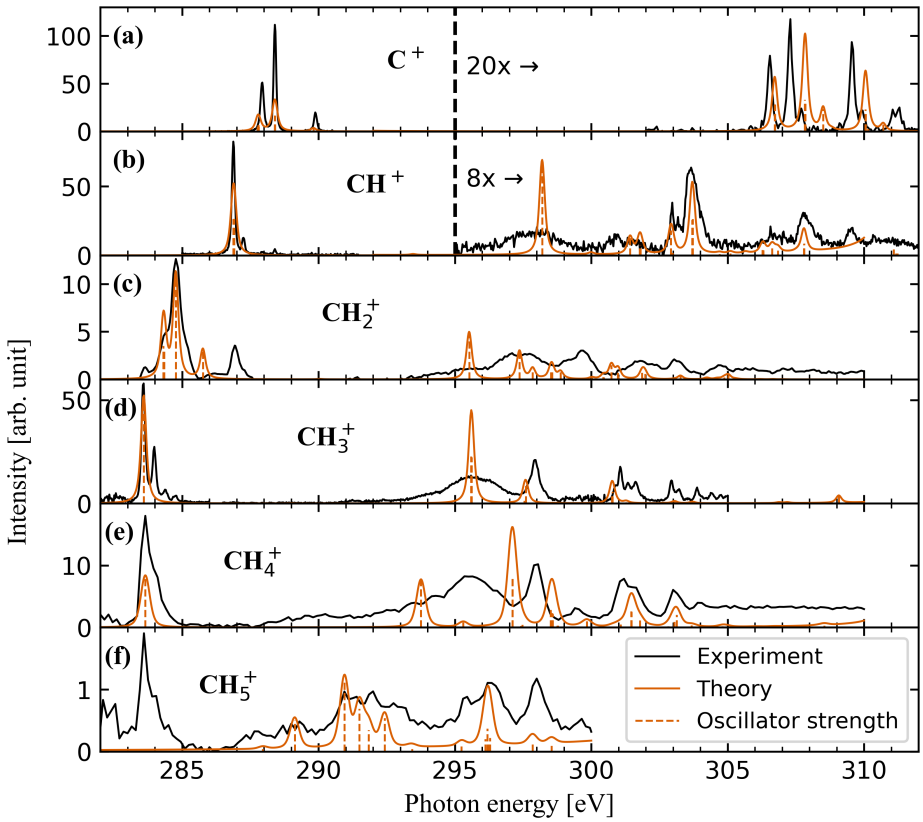

Figure 4.1: Measured XAS spectra (solid black) of the entire CH_n^+ series of ions (n=0-5). The spectra are accompanied by calculated spectra (solid orange), transition strength (dashed orange). Vibrations are not included.

progression appears, which should converge to the IP of the ion (double ionisation threshold for the neutral). This threshold lies just outside of the measurement. There are, however, a couple more peaks after some of the Rydberg series, these have been assigned as doubly excited states, similar to what was seen in N_2^+ [54].

Fluxionial structure of CH_5^+

One of the most interesting members of the CH_n^+ series is the exotic CH_5^+ ion. This is because from a basic chemistry perspective there are too many bonds for the number of electrons in the system. Unsurprisingly then the CH_5^+ ion is very unstable. Nonetheless it has been studied before, mainly to understand its structure [73, 74].

In Figure 4.1 the calculated spectra do not correspond very well with the experiment

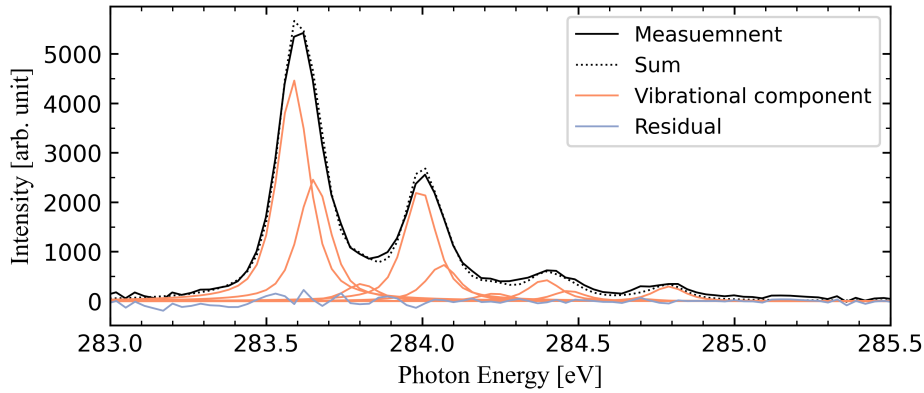

Figure 4.2: The π^* excited state of CH_3^+ vibrational modes. The experimental data is shown in solid black, while the fitted peaks are in solid orange, and the sum in dashed black. The fitting residual which was minimised is a solid blue line.

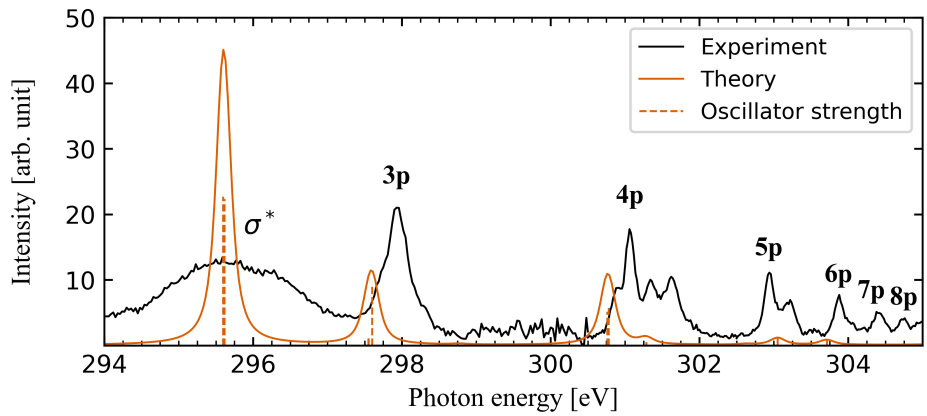

Figure 4.3: The higher energy states of CH_3^+, with both experimental and theoretical spectra. Assigned peaks are marked with their assignment.

for CH_5^+. We see that the first peak is not represented at all in the calculations. This is because much like in CH_4 the π orbital is full, and excitation of the C1s electron to the π is not possible. However, the experimental spectrum clearly contains the peak. The calculations were carried out for a symmetric geometry where each hydrogen is equally bonded to the carbon. Since Asvany *et al.*[73, 74] have shown that CH_5^+ is fluxional and thus oscillates between different geometries, we introduce two structures as shown in Figure 4.4, where A is the one previously mentioned (shown in C_{2v} symmetry) and structure B is a tripod structure with a H_2 moiety in C_s symmetry. With this additional structure the combined theoretical structure shows much greater agreement with the experimental data, as shown in Figure 4.5.

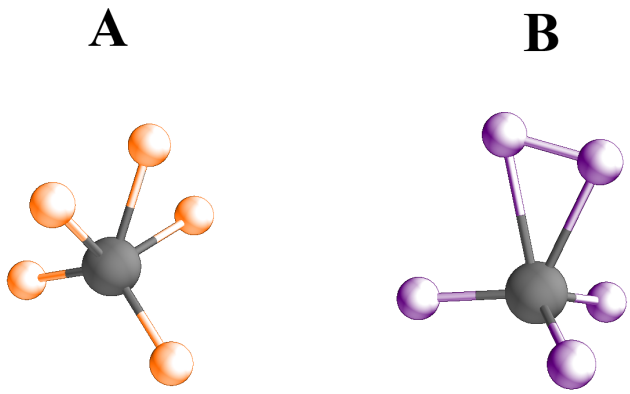

Figure 4.4: The two geometrical structures of CH_5^+. Hydrogen atoms are shown in orange for structure A and purple for structure B.

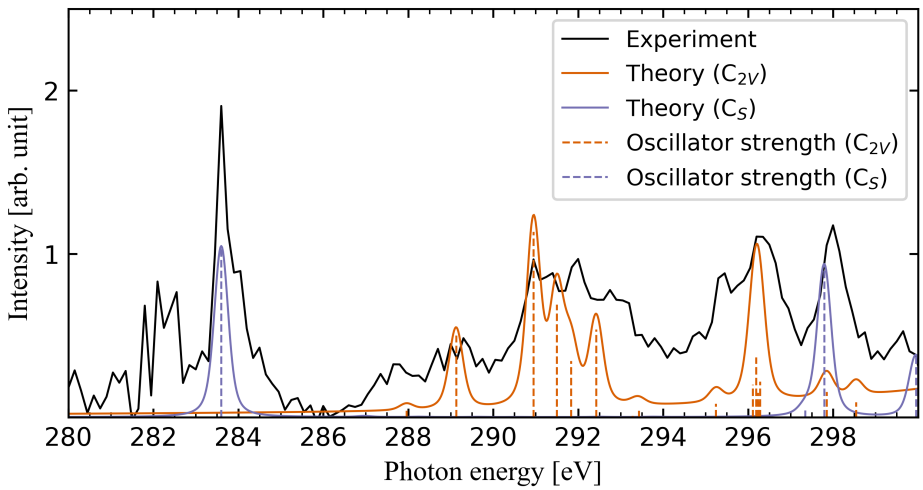

Figure 4.5: The experimental spectrum of CH_5^+ (solid black). Theoretical spectra of the two different geometries A (solid orange) and B (solid purple), with their transition state oscillator strength (dashed sticks of corresponding colour).

4.2 Resonant Auger-Meitner decay spectroscopy

Site-selectivity in gas phase molecules is an attractive concept for obtaining some control of the decay process. Selecting a specific atom on a molecule to be excited or ionised, then seeing an enhancement of a type of fragmentation or isomerisation would

mean that we can influence these dynamics. Core-excitation has been found to be highly site-selective depending on the chemical environment in the literature [75–81]. For low Z atoms the core hole is filled through the Auger-Meitner process. Therefore, the energy of the Auger-Meitner electron is an excellent observable to study the site-selectivity of resonant core excitation. In this section, Resonant Auger-Meitner spectroscopy will be presented in two different molecules, ethyl trifluoroacetate (ESCA) and cyclohexadiene (CHD), where site-selectivity is investigated.

4.2.1 Ethyl trifluoroacetate

The ESCA molecule, Figure 4.6, was made famous because it was the molecule used to first show chemical shift in a seminal book by Sigbahn *et al.* [82] in 1967. This showed how the carbon 1s electrons' binding energy depends on the chemical environment at each site in the molecule, here as CH_3, CH_2, COO, or CF_3. More studies on the ESCA molecule have been done with C 1s ionisation exploiting the site-selectivity. Auger-Meitner decay populates the same dication states in the ESCA molecule regardless of which carbon was initially ionised [83]. In addition, ion fragmentation after Auger-Meitner decay is not significantly affected by the site of initial ionisation [84]. This suggests that the memory of the original core-hole site is lost after Auger-Meitner transition.

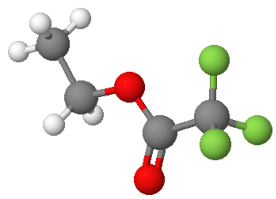

Figure 4.6: A 3D schematic of the ethyl trifluoroacetate (ESCA) molecule. The four carbon atoms are shown in grey, the five hydrogens in white, the two oxygens in red, and the three fluorines in green.

A recent study explored the C 1s near-edge X-ray absorption fine structure of the ESCA molecule, and the spectral features of resonant excited states could be assigned to different carbon sites [85].

These spectral features and their assignments are shown in Figure 4.7(a) together with

the total electron yield over the energy range. Figure 4.7(b) shows the 2D electron yield map scanned over both the photon and electron kinetic energies. In the 2D electron yield map three main types of contributions appear: direct ionisation of valence electrons, participator and spectator Auger-Meitner electron emissions. The direct valence emission disperses along diagonal lines, as the kinetic energy increases linearly with the photon energy. An inset on the right hand side of Figure 4.7(b) shows a valence electron spectra taken at 100 eV photon energy, and the valence states correspond very well to the diagonal lines. At some of the intersections between a diagonal (direct ionisation) and vertical (resonant excitation followed by Auger-Meitner decay) line, we can see an enhancement of intensity. We may then ask: why do we see this enhancement and is the fact that they primarily show up at strong resonances related to specific carbon sites relevant?

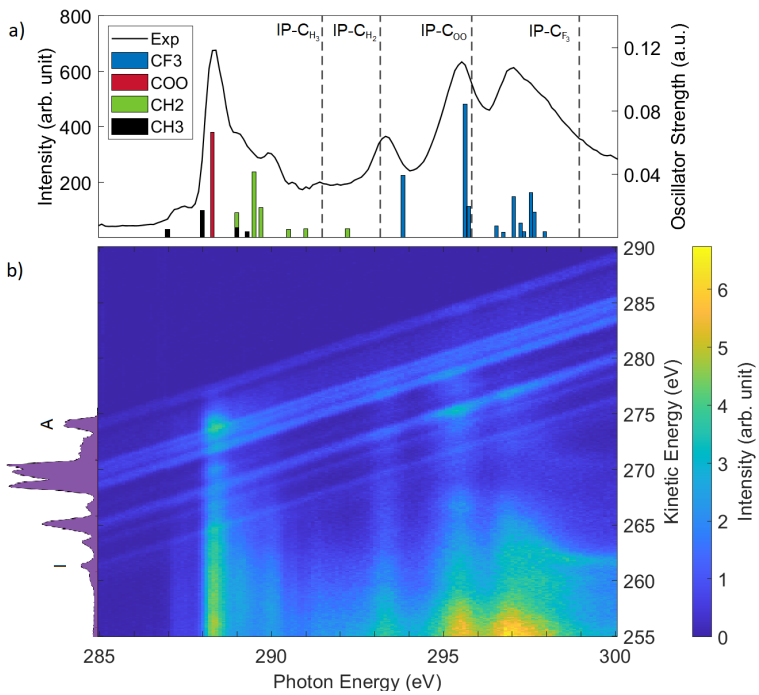

Figure 4.7: (a) An electron yield spectrum around the carbon C1s ionisation potentials and (b) a 2D Auger-Meitner electron emission map. Calculated oscillator strengths for the resonant transitions from the four different carbon sites are from ref. [85] (a). In the 2D electron map diagonal lines are visible, these are compared with the valence photoelectron spectrum placed on the left hand side (measured at 100 eV photon energy).

To resolve those questions theoretical calculations are used to obtain further knowledge about the transitions. Three resonant peaks are stronger and therefore chosen to be used in the calculations, these are at 288.3, 293.3, and 295.6 eV photon energy and correspond to COO 1s $\rightarrow \pi^*$, CF_3 1s $\rightarrow \sigma^*$, and CF_3 1s $\rightarrow \pi^*$,respectively.

Figure 4.8(a) shows the comparison of the experimental and theoretical data, which show excellent agreement. Furthermore, two points are marked X and Y, which show a significantly stronger enhancement. Figure 4.8(b) shows the spectra at the two resonances that contain the X (288.3 eV) and Y (295.6 eV) regions. The calculations reveal that the enhancement coincides with a strong overlap of the involved orbitals, as can be seen in Figure 4.8(c).

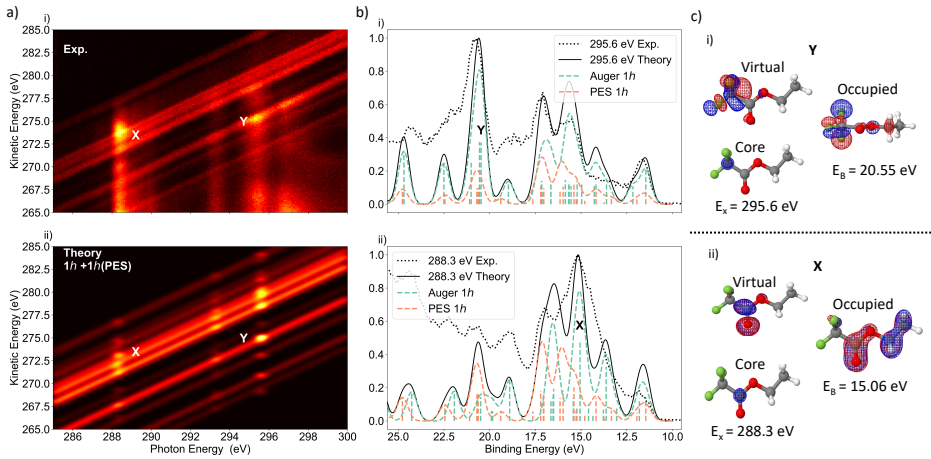

Figure 4.8: (a)(i,ii) Experimental and theoretical 2D Auger-Meitner electron emission maps. The theoretical maps contain off-resonant spectra (projected as diagonal lines) calculated at 288.3 eV by EOM-CCSD, and three resonant photoelectron spectra at 288.3, 293.3, and 295.6 eV photon energy. (b) The experimental (solid black line) and theoretical (dashed black line) spectra calculated for (i) CF_3 1s $\rightarrow \sigma^*$ excitation (at 295.6 eV) and (ii) COO 1s $\rightarrow \pi^*$ excitation (at 288.3 eV). The theoretical spectrum is the sum of the calculated Auger-Meitner (1h) channel (green dashed line) and the calculated direct photoionisation (PES 1h) channel (orange dashed lines), the oscillator strengths are presented as sticks of corresponding colour. (c) RASSCF neutral orbitals involved in the enhancement of (i) Y and (ii) X (Figure 4 in **Paper II**).

The combined experimental and theoretical study on the ESCA molecule reveals that if the core-excited and final state hole orbitals are spatially local to the absorbing carbon site, a strong enhancement of the transition signal is observed. This further reveals a strong site-selective probe in the Auger-Meitner decay electron emission for resonantly excited states.

4.2.2 Cyclohexadiene

Many cyclic molecules have biological significance, and shows up in a lot of important biological reactions in the human body. These biological molecules are usually very large, making them difficult to study, therefore it is beneficial to study their reactions using a prototype molecule. Such a cyclic prototype molecule is 1, 3-cyclohexadiene (CHD) which undergoes a ring opening under photon interaction to the linear 1, 3, 5-

hexatriene (HT) [86, 87]. In this section we explore the participator Auger-Meitner decay after resonant C 1s excitation, focusing on the π^* excited state and the different propensity for the Auger-Meitner decay at one of the three chemically different carbon sites.

Figure 4.9 shows the total ion yield of CHD around the K-edge and a 2D structure of the molecule. Six resonances are found and are assigned as shown in Table 4.1, A-B are of the same π^* state but of two different chemically shifted carbons, while C is vibrational substructure of both. Due to this chemical shift we can explore how the Auger-Meitner decay changes due to the site of the initial core-hole. Furthermore, we can capture the ion fragmentation arising from their transitions.

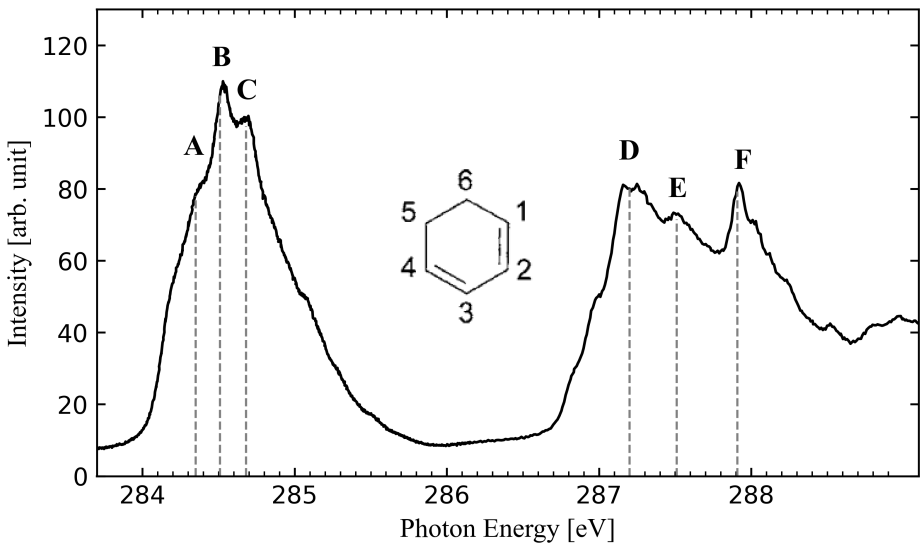

Figure 4.9: The total ion yield of the 1,3-cyclohexadiene molecule. Six resonant features are marked A-F. The 1,3-cyclohexadiene molecule is shown in the inset, where the different carbons are numbered.

Figure 4.10(a-b) shows the resonant Auger-Meitner spectra after excitation at the energies A-F. The states can be compared with the valence photoelectron spectrum and allow assignments shown in Table 4.2. Some differences can be noted; specifically we see that for the chemically different atomic sites there is a difference for the II and IV states, where the C(1, 4) has much higher propensity to decay to the 10b state. In 4.10(a) A-C have a feature slightly below 6 eV in binding energy, this feature is due to higher order harmonics from the synchrotron radiation ionising the C 1s. This is the only feature observed from higher order harmonics.

The Auger electron photo ion in coincidence (AEPICO) spectrum shows a very similar pattern for each resonant excitation (shown in **Paper III**), and each final state

Table 4.1: Inner-shell excited states in 1,3-cyclohexadiene. The energy and assignment of each peak is shown as well as the intensity ratio with respect to peak A.

Peak	Photon Energy [eV]	Assignment	I/I_A
A	284.35	$(C2, 3)$ - $1\pi^*$	1.00
B	284.49	$(C1, 4)$ - $1\pi^*$	1.42
C	284.68	vibrational substructure	1.31
	286.92	C 1s - $\sigma^*(C-C)$	0.828
D	287.30	$(C2, 3)$ - $1\pi^*$	0.828
E	287.51	$(C1, 4)$ - $1\pi^*$	0.751
F	287.91	C 1s -σ^*(C-H)	0.841
IP	289.91	$(C1, 4)$-∞	-
IP	290.14	$(C2, 3)$-∞	-
IP	290.50	$(C5, 6)$-∞	-

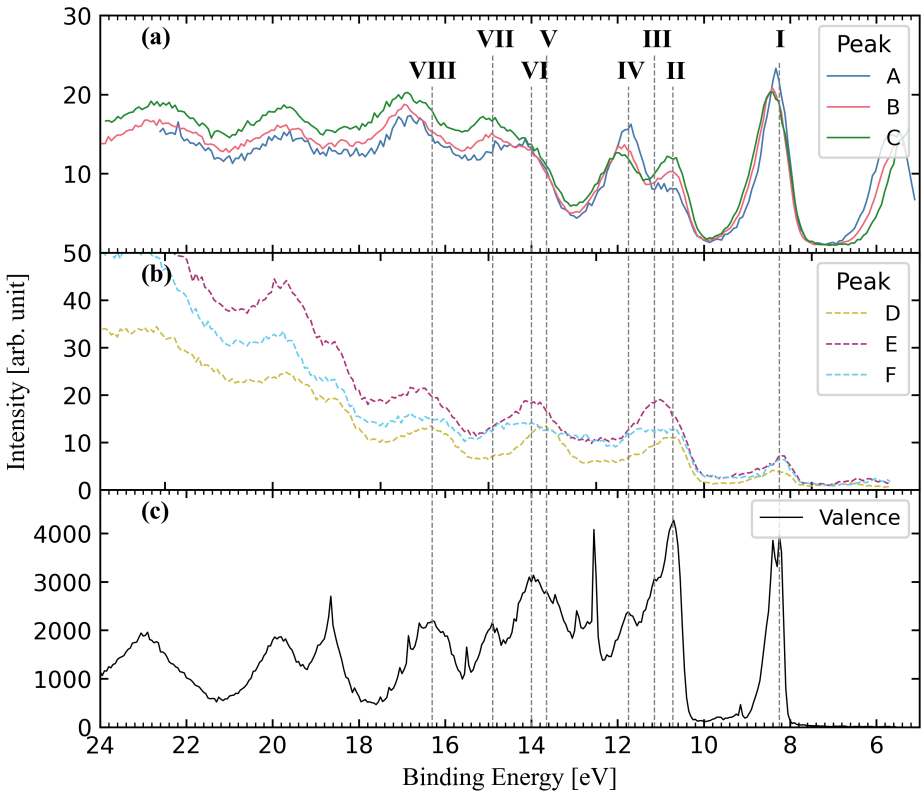

Figure 4.10: Resonant Auger-Meitner spectra for resonant feature A-C (a) and D-F (b), as well as a photoelectron spectrum in the valence region taken at 100 eV photon energy (c). The six Auger-Meitner spectra are taken at the six resonant features indicated in Figure 4.9. All spectra are plotted in binding energy scale so that they can be compared, and specific states of interest are marked I-VII.

corresponds to the same fragments regardless of initial excitation. In other words, each Auger-Meitner decay corresponds to a set of mass fragments, and this does not

Table 4.2: Valence electronic states in 1,3-cyclohexadiene. All states correspond to one-hole molecular orbitals (MO) which are taken from the assignment in ref. [88].

Peak	Binding Energy [eV]	MO	Character
I	8.25	11a	$\pi_{C=C-}$
II	10.72	11b	$\pi_{C=C+}$
III	11.15	10a	σ_{CC}
IV	11.75	10b	σ_{CC}
V	13.65	9b	σ_{CC}
VI	14.0	8b,8a	σ_{CH-},σ_{C-C},$\sigma_{C=C}$
VII	14.9	7b	π_{CH_2}
VII	16.3	6b,7a	C_{2s},σ_{CH+}

change when a different initial resonant excitation or carbon site is used. However, Figure 4.11 shows which fragments are associated with which Auger-Meitner decay. It has been reported that at the conical intersection traversed during the CHD $\rightarrow$ HT conversion a hydrogen loss is common [89]. This would suggest that mass 79 amu is associated with this dynamical process. From Figure 4.11 we can deduce that it is primarily state III and IV where a fragment with mass 79 amu is found. This suggests that the resonant states with high intensity in that Auger-Meitner decay has high probability of entering this conical intersection. Furthermore, this indicates that an excitation of the C$(1, 4)$ enhances the ring-opening, even though the bond breaking occurs in C$(2, 3)$. This is suggested to be because the dynamic is through rotation of the double bonds, creating a torsion movement [90].

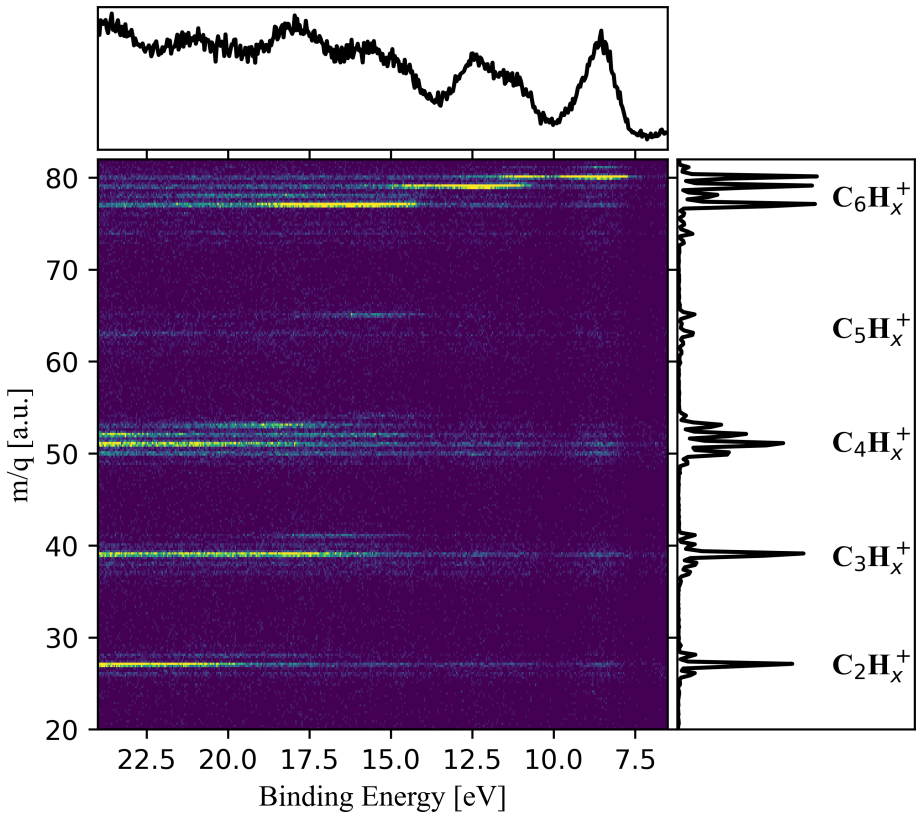

Figure 4.11: The AEPICO map measured at feature B. The integrated Auger-Meitner spectrum is shown at the top, while the integrated mass spectrum is shown on the right.

4.3 Dynamics of photoexcited and photoionised cyclopropane

Cyclopropane is the smallest cyclical hydrocarbon with the carbon atoms forming an equilateral triangle in the ground state (see Figure 4.12). Cyclopropane is more reactive than other cyclical hydrocarbons due to the ring strain arising from the less than optimal overlap of the sp^3 hybrid orbitals in the ring system. The unique ground state electronic configuration of cyclopropane is responsible for its anomalous properties [91].

A recent study of the coupling between the electronic states in the dication and two-body fragmentation revealed that populating certain electronic configurations in the inner-valence region increased the propensity for isomerisations leading to specific fragmentation [92]. In short, excitation leads to Jahn-Teller distortion leading to a symmetry reduction from D_{3h} to C_{2v} with corresponding energy split states[93–

95]. This distortion elongates either one bond creating an isosceles triangle with two angles below 60 degrees or two bonds are extended and two angles increase. Oghbaie *et al.* suggested that certain dication states could act as gateway states for pathways into one of these distorted geometries [92]. This was explored by core excitation in **Paper IV**, with the idea that by first exciting an electron to the anti-bonding states an isomerisation would be initiated, and when the Auger-Meitner decay occurred in the altered geometry population of dilation states leads to specific fragmentations. That indicates both the geometry and eventual angular anisotropies in fragment emission could reveal the imposed dynamics.

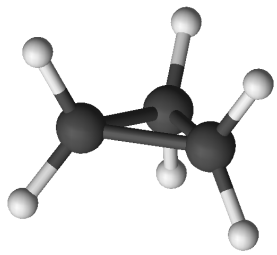

Figure 4.12: A 3D view of the cyclopropane molecule, the carbons are viewed in grey and hydrogens in white.

4.3.1 State selectivity

The first step into exploring the aforementioned hypothesis is by understanding the C 1s excited states. Figure 4.13 shows an ion yield around the K-edge. Hitchcook and Sze *et al.* [96, 97] assigned many of the features in the ion yield from their inner shell electron energy loss spectroscopy ISEELS spectra and calculations. The empty orbitals around the ionisation potential are:
$(4a_1')(2a_2'' \ \pi^*)(1a_2' \ \sigma^*_{ex})$(I.P.)$(4e' \ \sigma_{in}{}^*)(2e_2'' \ \pi^*)(5e' \ \sigma_{in}{}^*)$. Furthermore, Duflot *et al.* calculated the geometries after excitation to these states, and suggested that the geometrical relaxation of cyclopropane is sensitive to the bonding character of the valence molecular orbitals [98]. Notably, in the $1a_2'$ state the electron density is situated on a single CC bond, while in the $5e'$ state the electron density is spread over the entire triangle. Because both of these orbitals are anti-bonding, it can be hypothesised that $1a_2'$ initiates a single bond elongation and $5e'$ initiates two bond elongation.

The ICE spectrometer was used in this experiment and the ions and electrons were collected in coincidence for each resonant state, and two off-resonance energies (one above and one below). Figure 4.14 shows a typical mass spectrum from the measurements, all m/q peaks were present in every measurement but their intensities varied. Notably, we see that at 42 amu there is a small peak which corresponds to the parent

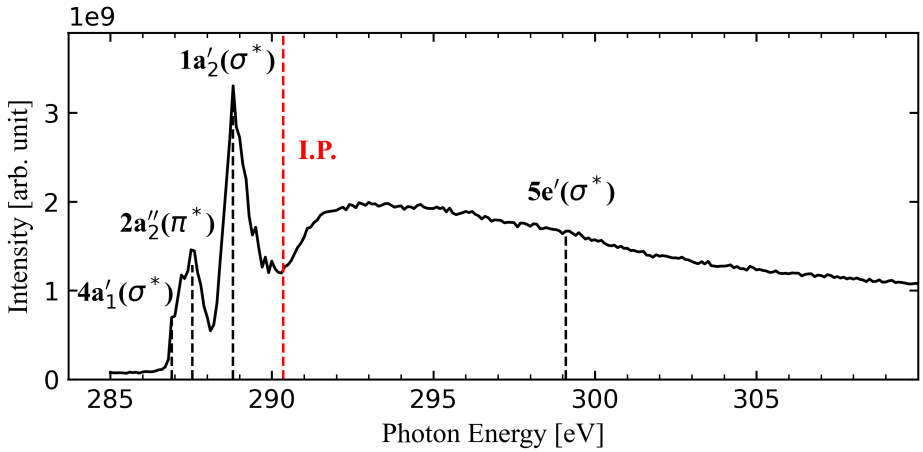

Figure 4.13: The total ion yield of cyclopropane around the C 1s ionisation edge (marked by a red dashed lined and I.P.). Three visible resonant features are marked, while the 5e″ excited state is marked but not visible. The energy of the 5e″ state is obtained from theoretical calculations.

ion, $C_3H_6^+$. Five other groups are visible, the first group at $1-3$ Da corresponds to H^+, H_2^+ and H_3^+. The second, fourth and fifth groups correspond to C-based, C_2-based and C_3-based fragments, respectively. In those groups, each peak is broader, reflecting a higher kinetic energy in the dissociation. This is expected as the spectrometer is optimised to capture the 3D momentum images rather than pure mass spectra. The third group with very narrow peaks at $18.5-20.5$ Da are dications that have not dissociated.

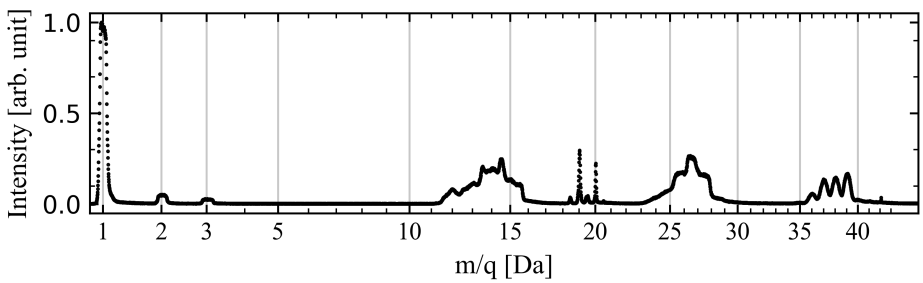

Figure 4.14: Mass spectrum of cyclopropane after ionisation with 299.1 eV photon energy, above the ionisation edge.

Figure 4.15 shows the TOF correlation maps of coincidence events with two ions in two regions of interest. When studying the dynamics of ion dissociation, it is advantageous to have captured all or at least almost all of the fragments. Because of this fragment pairs (1)-(6) are chosen for a closer inspection, these also have the lowest appearance energy in dissociation of the dication from valence ionisation [92].

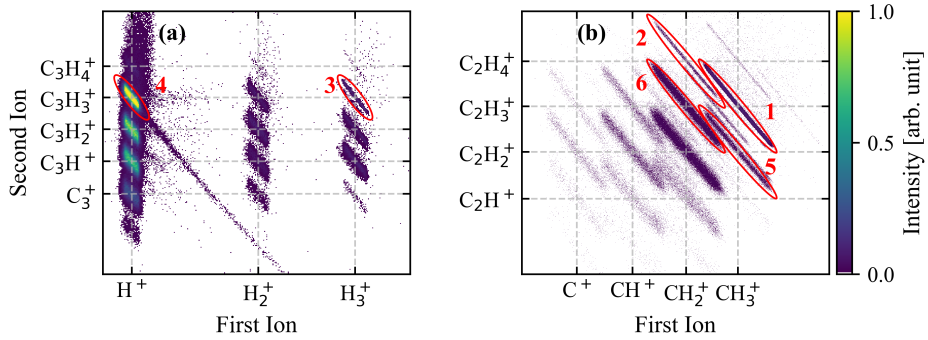

Figure 4.15: Ion-ion correlation maps of two regions of interest. (a) Fragmentation pairs were no carbon-carbon bond has been broken $H_n^+/C_3H_m^+$ (n=1-3, m=0-4), and (b) fragmentation pairs were at least two carbon-carbon bonds have broken $CH_n^+/C_2H_m^+$ (n=0-3, m=1-4). Pairs with special interest are marked and numbered.

Using the theoretical work outlined by Oghbaie *et al.* [92], we find that (2) $CH_2^+/C_2H_4^+$ dissociates through two CC bonds elongation, and (1) $CH_3^+/C_2H_3^+$ dissociates through a single CC bond elongating followed by a hydrogen migration. Furthermore, it can be extended that (6) $CH_2^+/C_2H_3^+$ should follow the same path as (2) and (5) $CH_3^+/C_2H_2^+$ the same as (1). Pair (3) $H_3^+/C_3H_3^+$ was initially suggested to form H_3^+ by three simultaneous CH bond breaks via vibrational modes. However, this was later questioned by Kwon *et al.* [99], who suggested that the formation was instead linked with roaming. This notion of a roaming mechanism was therefore further investigated and both (3) and (4) $H^+/C_3H_3^+$ become involved in this roaming pathway, which is discussed further and more in depth in the next section.

The theoretical outline then suggests that (1) and (5) should increase in intensity at the $\sigma^*(1a_2')$ resonance due to the electron density being concentrated at a single CC bond. The pairs (2) and (6) propensity should increase at the $\sigma^*(5e')$ due to the electron density being spread over the entire molecule. Table 4.3 shows that this is not quite the case, instead we see little change at those resonances. The one exception is a sharp increase of (1) at the $\sigma^*(5e')$ resonance, however, due to the fact that this increase remains at the off-resonant energy the more likely explanation is that the propensity for this fragmentation increased after the ionisation edge rather than an imposed isomerisation due to state-selectivity.

The anisotropy (β) is a useful parameter in resolving how molecules dissociate [100]. Figure 4.16 shows the β-parameter for five fragment pairs. (4) is not shown because it is formed by two contributions which will be explained later. The β parameter for (3) shows clear isotropy, this would be in stark contrast to what would be expected if three hydrogen bonds broke at the same time. If that were the case one would have a β showing the fragment dissociating perpendicular to the triangular plane. The isotropic

Table 4.3: The normalized intensity of the fragmentation channels (1)-(3) and (5),(6) over the measured energies with given character. The photon energies 285 and 315 eV are off resonance.

	285 eV	$\sigma*(4a'_1)$	$\pi*(2a''_2)$	$\sigma*(1a'_2)$	$\sigma*(5e')$	315 eV
(1) $CH_3^+/C_2H_3^+$	0.4024	0.4174	0.3847	0.3877	0.5170	0.5144
(2) $CH_2^+/C_2H_4^+$	0.1085	0.1358	0.1313	0.1309	0.0556	0.0784
(3) $H_3^+/C_3H_3^+$	0.0156	0.0177	0.0174	0.0170	0.0176	0.0176
(5) $CH_3^+/C_2H_2^+$	0.1330	0.1500	0.1684	0.1601	0.1217	0.1488
(6) $CH_2^+/C_2H_3^+$	0.3406	0.2791	0.2982	0.3044	0.2881	0.2408

behaviour however is consistent with roaming, as this is a very slow process (allowing rotation before dissociation). All the other four channels show similar behaviour, positive for σ^* and negative for π^*. This means the dication is dissociating in the same plane as the triangle was when it interacted with the photon. We can see some difference, (1) and (5) follow each other and are both more isotropic than (2) and (6), which also follow each other. This suggests that they indeed follow the corresponding dissociating pathway as outlined before, but also that (1) and (5) most likely have a slower dissociation, allowing some rotation. This is not surprising, as a proton migration must occur to create the CH_3^+ fragment.

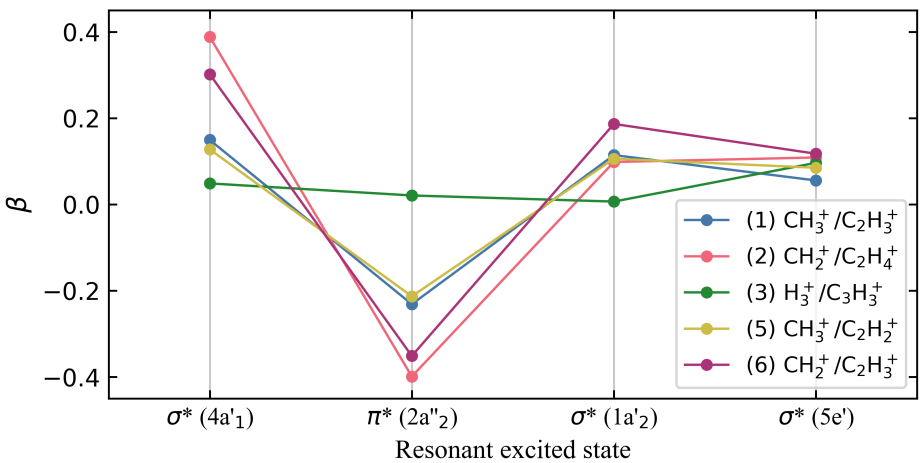

Figure 4.16: Anisotropy, β, for five fragmentation pairs over four resonant excited states.

These results indicate that the core excited state does not initiate the isomerisations that were suggested. However, due to the similarities one can instead expect that each fragmentation starts from the same geometry, an open ring from a single bond elongation. This is suggested from the core-equivalent structure calculated at the $1a'_2$ state by Duflot *et al.*[98], were a carbon-nitrogen-carbon open ring structure was found (nitrogen being Z+1 equivalent to carbon due to the ionisation of an electron). This means that instead of state-selective, the process is site-selective and breaks the CC

bond opposite the core-excited carbon. Site-selectivity is well studied [75, 79–81, 101], but is usually very difficult to study in a symmetric molecule like cyclopropane as each carbon is chemically identical.

4.3.2 Roaming mechanism

As mentioned previously, Kwon *et al.* [99] suggested that the H_3^+ formation was due to roaming, specifically a neutral H_2 moiety roams around the $C_3H_4^{2+}$ dication. This was discerned from a time-resolved experiment where the time from double ionisation of cyclopropane to when H_3^+ was formed was measured. In cyclopropane 249 fs and in propene, a linear isomer, 225 fs was found [99]. The difference was assigned to the extra time it takes for cyclopropane to open and become linear like propene, which was supported by calculations. Furthermore, Mishra *et al.* [102] investigated the roaming process in the dication of acetonitrile (CH_3CN^{2+}) using momentum imaging. They used an interrupted roaming channel $H^+/CCN^+/H_2$ where the H_2 was roaming but the dication dissociated before it could abstract a H^+. The H_2 momenta were reconstructed to obtain a complete picture, which they saw as a fingerprint of roaming. An equivalent channel exists in cyclopropane, namely (4) $H^+/C_3H_3^+$ where H_2 is missing. Therefore, channels (3) and (4) are used in the roaming investigation.

The Dalitz plot [103–106] is a useful tool for determining the fragmentation mechanism and especially how the KER is distributed in a three-body fragmentation. The coordinates in phase space are defined using normalised coordinates

$$x = \frac{\varepsilon_{P_3} - \varepsilon_{P_2}}{\sqrt{3}} \tag{4.1}$$

and

$$y = \varepsilon_{P_1} - \frac{1}{3} \tag{4.2}$$

where the normalised squares of the linear momentum ε_{P_i} of each ion i is

$$\varepsilon_{P_i} = |\mathbf{P_i}|^2 \,/\, \sum_n |\mathbf{P_n}|^2 \tag{4.3}$$

for all n ions. The key to the Dalitz plot is that the data points under these coordinates will have to satisfy two constraints. Firstly, due to the normalisation

$$\sum_i \varepsilon_{P_i} \equiv 1 \tag{4.4}$$

the three particles are energetically constrained to lie on a triangular plane that intersects the energy maxima, $\varepsilon_{P_i} = 1$ in a Cartesian coordinate system. Secondly, the

momentum

$$\sum_i \bar{P}_i \equiv 0 \tag{4.5}$$

is constrained due to the conservation of linear momentum. These constraints limit the data points to a circular area inscribed in the triangle, thus the maximum value for the normalised squared momentum vectors is $\varepsilon_{P_i,max} = \frac{2}{3}$. Figure 4.17 shows how the Dalitz plot is formatted and how the magnitude of the different momentums will place the data points.

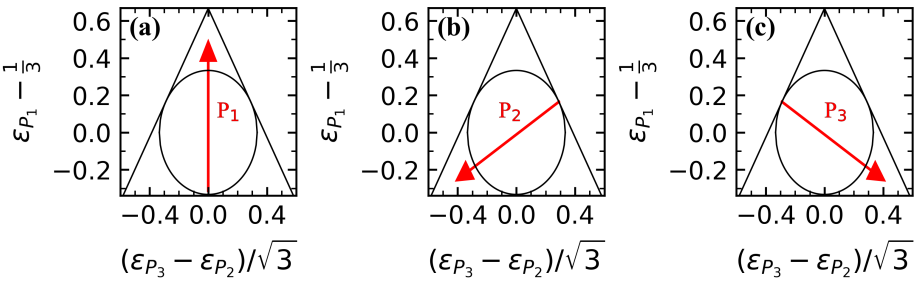

Figure 4.17: Schematic view of the momentum components in a Dalitz plot. The red arrow shows which coordinate is gained with increase of (a) P_1, (b) P_2, and (c) P_3.

The Dalitz plot is a good tool to determine the fragmentation dynamics, but it says nothing about the momentum vector's direction in space. This is where the Newton diagram is invaluable for presenting the correlation of the linear momentum in the molecular frame [107, 108]. In a three-body fragmentation process the three vectors are necessarily coplanar, meaning that they span one unique plane, the vectors on this plane can therefore be plotted in a 2D diagram. This is done by first rotating all of the vectors such that one of them aligns with the x-axis, then the vectors are rotated around the x-axis such that the two remaining vectors land on the xy-plane. It is important that one of the vectors always falls on the upper half ($P_y > 0$) which makes the third vector automatically fall on the lower half ($P_y > 0$), as depicted in Figure 4.18(a). This is done for each fragmentation event and the momentum vectors from a measurement can thus be drawn as a histogram. Figure 4.18(b) shows an example of how a sequential break-up would appear, where the P_2 and P_3 momenta are anti-correlated such that they create a ring with respect to P_1.

Figure 4.19 shows the momentum distribution of $H^+/H_2/C_3H_3^+$, and it is very similar to acetonitrile, suggesting that the H_3^+ formation indeed follows a similar pathway. However, within the distribution, particularly in Figure 4.19(b) for the H^+ fragment, it is clear that there are two parts: one part with higher KE that have a single angle with respect to $C_3H_3^+$, and a lower constant KE part with an angle to $C_3H_3^+$ that

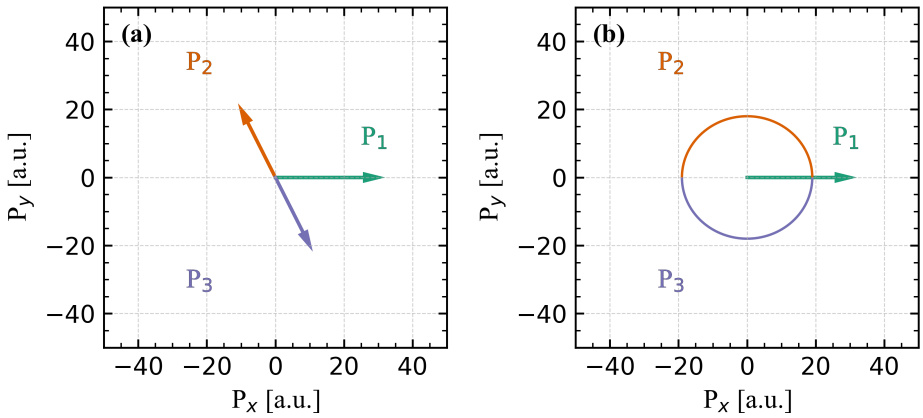

Figure 4.18: (a) The coplanar vectors that make of a Newton diagram, where the P_2 and P_3 are aligned on the basis of P_1, and then rotated to lie on the positive ($P_y > 0$) and negative ($P_y < 0$) half plane, respectively. (b) An example of how the P_2 and P_3 distributions spread out when a sequential fragmentation occurs and the P_1 is the fragment emitted in the first step.

changes. The angular dependence in this case is on the H_2 fragments angle with respect to $C_3H_3^+$. We therefore investigate these further.

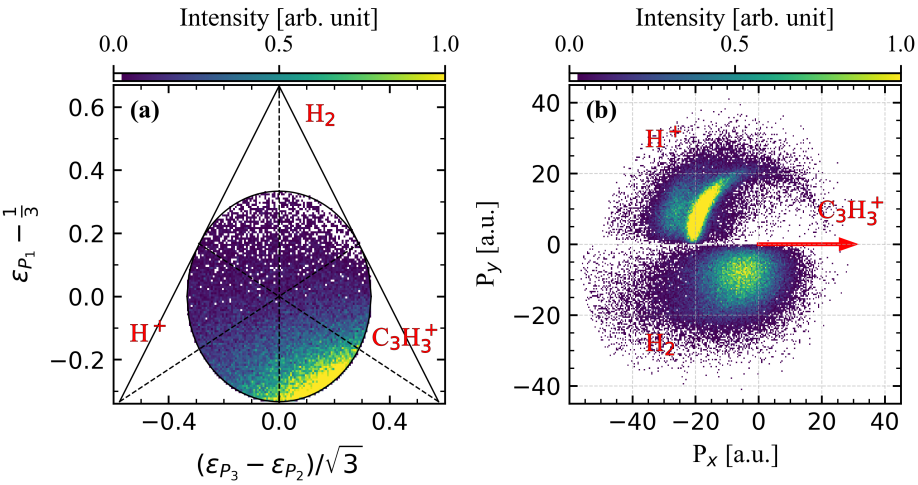

Figure 4.19: (a) The Dalitz plot of the channel $H^+/H_2/C_3H_3^+$, where ε_1, ε_2, ε_3 correspond to H_2, H^+, $C_3H_3^+$, respectively. (b) A Newton diagram with the heaviest $C_3H_3^+$ fragment aligned with the x-axis.

Because there seems to be a difference in KE, a comparison in the total KER is made with the KER of the charged fragments. This is because usually with a three-body fragmentation where one of the fragments is neutral the neutral part will have almost no KE and the charged pair will experience an almost two body Coulomb explosion.

Figure 4.20 shows this KER correlation, and it is clear that there are two distributions. The two distributions are assigned as the X and Y channels, where X has a constant KER between the two charged fragments at all total KER values. This means that all the rest of the KE is distributed onto the H_2. On the other hand, for the Y channel the two charged fragments carry all the KE even as the total KER increases, leaving the H_2 with almost no KE. The two channels overlap considerably at the lower total KER, but can be separated above 6 eV.

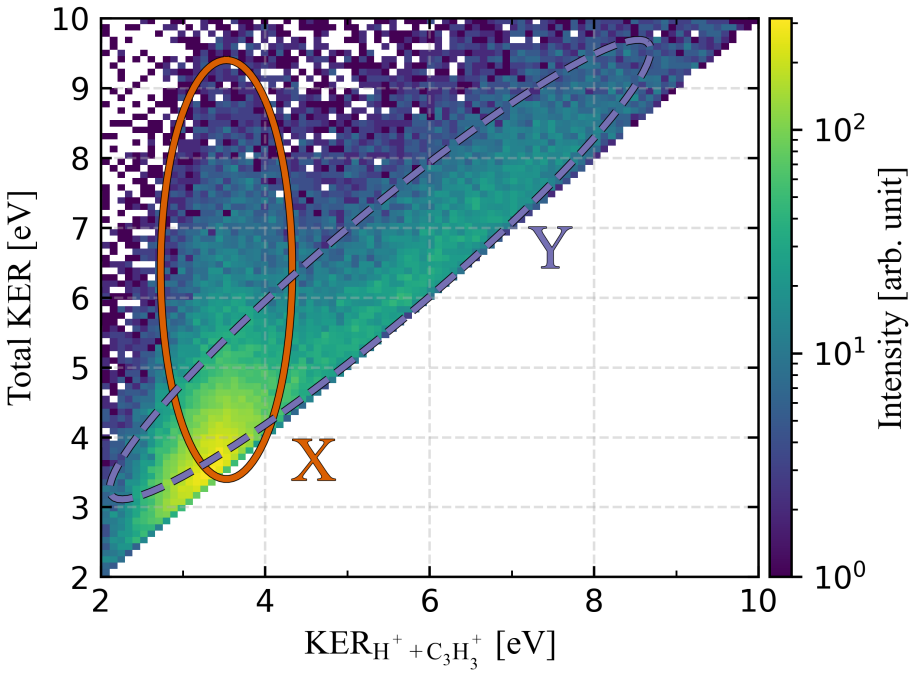

Figure 4.20: A kinetic energy release correlation diagram for the fragmentation channel $H^+/H_2/C_3H_3^+$. The kinetic energy between the two charged fragments is plotted against the total kinetic energy release. Two regions showing two different channels are marked as X (solid orange) and Y (dashed purple).

Figure 4.21(a) shows the Dalitz plot after a KER filter of KER_{Total}>6 eV has been applied. The two channels which were hidden are now clearly visible in Figure 4.19(a). The Y channel is characterised by a asynchronous concerted dissociation while the X channel show signs of a sequential breakup. However, the X channel seems to have lower intensity for lower H_2 KE. The Newton diagram for the Y channel in Figure 4.21(b) clearly shows that the higher KE part of H^+ with less angular dependence seen in Figure 4.19(b) is due to this channel. Furthermore, it can be seen that this is associated with a broad and low KE distribution of the H_2, typical of a concerted dissociation. Figure 4.21(c) then displays the low KE contribution of H^+ with more

angular dependence belongs to the X channel. The H_2 has a higher KE and a very narrow angular distribution relative the other fragments. From this we conclude that the X channel is due to the roaming mechanism. Specifically it suggest that the bond which breaks to create the two charged fragments always releases the same amount of energy. Which is transferred to the H_2, we suggest that the source of this energy is a vibrational mode involving CH. This is in line with the mechanistic view presented by Mishra *et al.*[102]. The CH bond breaks spontaneously during the roaming process, redistributing the excess energy to the roaming neutral H_2.

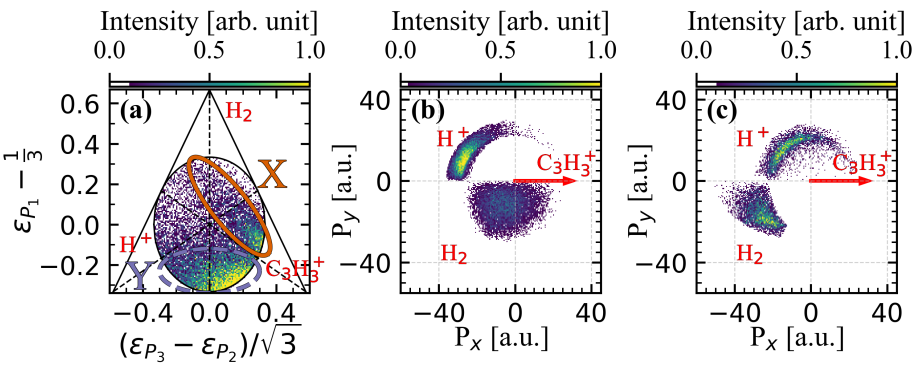

Figure 4.21: (a) Dalitz plot for the kinetic energy filtered (KER_{Total}>6) fragmentation channel $H^+/H_2/C_3H_3^+$. The X and Y channel are marked, and filtered to give two data sets. Newton diagrams shown for channel (b) Y and (c) X, where the $C_3H_3^+$ fragments momentum vector is aligned with the x-axis.

With the previous discussion in mind one can then consider how H_3^+ forms in this process. The bond between H_2 and H^+ that allows the formation of H_3^+ requires energy, around 4.35 eV [109]. We can, with that in mind, add this bond formation energy to the dissociation energy of $H_3^+/C_3H_3^+$ to obtain the total internal energy required for this process. This is shown in Figure 4.22, where the bond energy is broadened by a Gaussian of the same width of the measurement resolution. With these energies we can construct a KER correlation map between the charged fragments and this new total KER that includes the internal energy need to form H_3^+. Figure 4.23(b) shows this KER map, further more we can add the interrupted roaming channel $H^+/H_2/C_3H_3^+$ (Figure 4.23(a)) to get a summation in the KER correlation (Figure 4.23(c)). We see that the added energy "fills" out the X channel at the higher total KER energies. Figure 4.24 shows the branching ratios above 6 eV total KER with all three channels. As the X channel decrease at higher total KER the successful roaming channel takes over. The fact that the Y channel stays constant to these two suggest that it is the X channel being converted into the H_3^+ channel at the higher energies. In essence when higher energies gets deposited onto the H_2 there comes a point were the H_2 gets enough energy to bond to the dissociating H^+ forming the H_3^+ product.

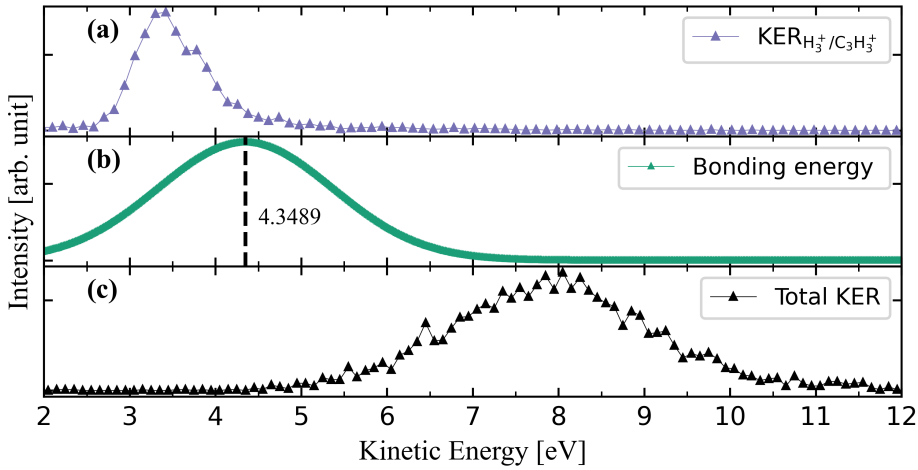

Figure 4.22: (a) The Kinetic energy release of the $H_3^+/C_3H_3^+$ pair, with (b) the associated H_2 and H^+ bond energy broadened by a Gaussian equivalent with the energy resolution. (c) The kinetic energy release includes both contributions.

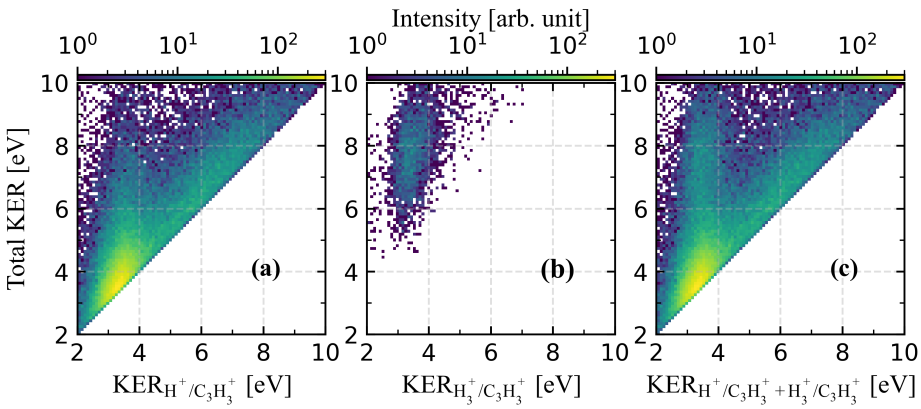

Figure 4.23: Kinetic energy release correlation diagrams for (a) $H^+/C_3H_3^+$ and (b) $H_3^+/C_3H_3^+$ with a total kinetic energy release described in the text. (c) The two aforementioned diagrams are added together to create the sum of both channels.

The roaming mechanism in cyclopropane is then able to form the H_3^+ ion by having enough energy within a vibrational CH bond. The X channel shows what occurs when the energy is not enough and the roaming neutral, H_2, is ejected with all the excess energy that was not needed to dissociate the fragment pair $H^+/C_3H_3^+$. This channel competes with Y, and the unsuccessful (interrupted) roaming channel with the successful roaming channel have a constant ratio of 0.65:0.35.

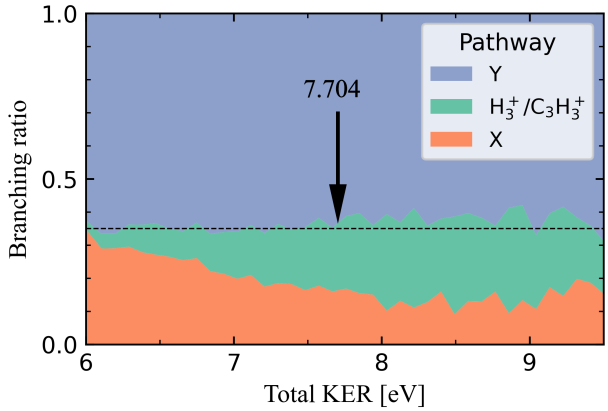

Figure 4.24: The branching ratio of the three involved channels above 6 eV total kinetic energy release. A dashed line at 0.35 shows that the branching ratio between Y and the rest is constant. The theoretical activation energy for H_3^+ formation from H_2 and H^+ is shown with an arrow.

4.3.3 Triply charged fragmentation

The cyclopropane experiment was one of the first beamtimes with the newly commissioned ICE spectrometer. Therefore, the capability of the spectrometer was further explored by looking at how well the momentum and KER could be explored in the triply charged fragmentation. One strong three-body channel, $H^+/CH_2^+/C_2H_3^+$ was chosen. This channel has been studied using ion collisions by Lin *et al.* [110], who found that there were two different sequential fragmentation pathways for this three-body channel. A photon energy of 299.1 eV was used (above the C1s ionisation edge) with the lens mode of the spectrometer, described in Section 3.2.4.

The ions in coincidence are selected in a 3D diagram (not shown) where the xyz-coordinates are replaced by TOF of the first, second, and third ion hit of an event. Figure 4.25 shows the KER sum of the two heavier fragments in relation to their angle with the proton, in the native frame [108]. This clearly displays the two pathways, named I and II, and allows each pathway to be selected and thus filtered out of the dataset. The Newton diagram can then be used to show both that they follow a sequential dissociation but also in which order the fragmentation occurs. In Figure 4.26(a) we present the Newton diagram for pathway I with the proton aligned with the x-axis. The other two fragments create a clear circular distribution relative to each other, which suggests sequential dissociation where the proton is emitted in the first step. Figure 4.26(b) shows pathway II in a similar manner, but here the CH_2^+ fragment is aligned with the x-axis. This confirms that the sequential break up is as follow:

Pathway I: $C_3H_6^{3+} \rightarrow C_3H_5^{2+} + H^+ \rightarrow CH_2^+ + C_2H_3^+ + H^+$

Pathway II: $C_3H_6^{3+} \rightarrow C_2H_4^{2+} + CH_2^+ \rightarrow H^+ + C_2H_3^+ + CH_2^+$.

Furthermore, this analytical procedure allows very precise determination of the reactions KER, as shown in Figure 4.27. The KER and the assignment of the fragmentation channels pathway agree very well with previous studies on cyclopropane with ion collisions [110].

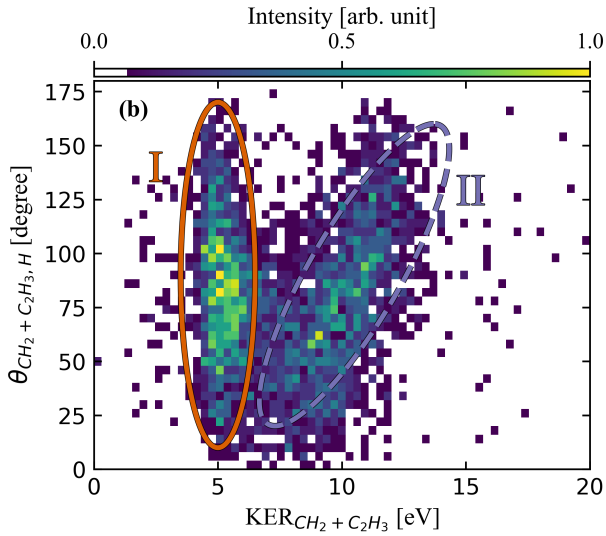

Figure 4.25: Native frame plot of the $H^+/CH_2^+/C_2H_3^+$ channel, here the KER of the two heavier fragments are plotted against the angle between them and the third fragment H^+. Two regions are marked, I (solid orange) and II (dashed purple) for the two different distributions.

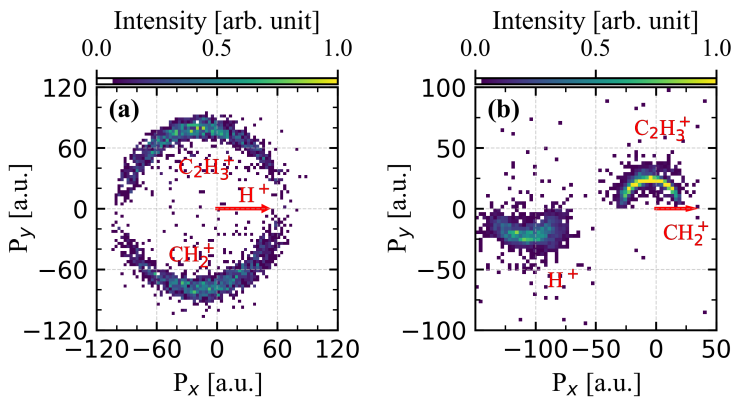

Figure 4.26: Newton diagrams of Pathway I (a) and Pathway II (b).

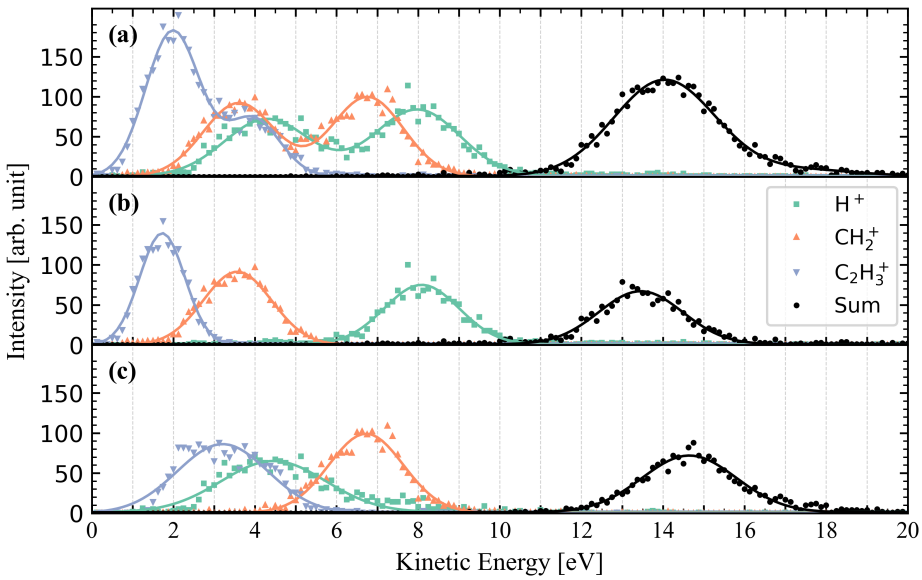

Figure 4.27: The kinetic energy release of the (a) complete fragmentation channel as well as for pathway I (b) and pathway II (c). The data is shown as markers while a Gaussian fit is shown in a solid line for each energy peak.

Chapter 5

Summary and outlook

The thesis work set out to study inner-shell excitations and ionised molecules both in a neutral and charged initial state. This work furthers the understanding of the dynamical processes that can occur on the excited potential energy surfaces in the ultrafast time regime. The studies used different methods and instruments to gain knowledge from a variety of perspectives. Central to the studies was the synchrotron radiation, as it is currently the only source capable of allowing all the studies this work conducted with the shown result. This highlights both the versatility of synchrotron radiation, and the many avenues in physics that can be explored with this light source. This last chapter will provide brief concluding summaries of the included papers and a look at future questions that this work raises.

XAS on ions

The XAS on ionic molecules provides a novel view of inner shell electronic structure. New state transitions may appear in comparison to the neutral molecule. Due to a different ionisation potential threshold (double ionisation) a clearer picture may be obtained for certain states. An example is σ^* shape resonances that have been seen to "fall" below the ionisation threshold in the ionic XAS.

The CH_n^+ series showed spectroscopy on species very difficult to study because they are highly reactive or unstable. Moreover, evidence for fluxional structures of CH_5^+ was shown and for the first time XAS spectra of the two molecular geometries of the fluxional cation could be observed.

Part of the studies during this thesis work were dedicated to an ion trap called TRISS that will be available at MAX IV. Commissioning has started, but no results were yet

achieved and thus it was excluded from this thesis. This new ion trap aims to provide greater control of the trapped ions, allowing them to be moved from and to different chambers that can interact with synchrotron radiation, electron gun, or a contraction of the trapping fields causing collisions. A reflectron TOF spectrometer is used to detect the final fragments much like the Berlin setup described in section 3.2.1. This should mean that new ions can be studied with more complex initial status.

Auger-Meitner decay

The site-selectivity of Auger-Meitner decay was in focus in this thesis, and indeed in both the ESCA and CHD molecules, clear differences between transitions from different sites were observed. The ESCA molecule showed that the functional group could be identified using the resonant Auger-Meitner spectrum, opening the avenue to investigate larger biomolecules (i.e. amino acids) through site-selectivity, which could be combined with ion TOFs to understand how they fragment under UV radiation as an example. In CHD the simple picture once developed for the CHD→HT becomes increasingly complex, with resonant LUMO+1 excitation shown to indicate a strong propensity for this dynamic ring opening.

The roaming mechanism

The momentum imaging provided clear evidence of the roaming mechanism being responsible for the formation of H_3^+ from the cyclopropane dication. Moreover, we could show the importance of the internal energy and connect it to the CH vibration, which is required for the roaming mechanism in cyclopropane to successfully abstract a proton. The dynamics of the two channels, X and Y, indicated agreement with the theoretical models that have been developed in the literature.

One of the main aspects of the roaming mechanism has been that the neutral roamer is quasi-bound on a very shallow potential energy surface. The implication of a vibrational mode and the emission and rebinding of the roamer indicate that there may be more to the story. The knowledge of this vibration, how it affects the potential energy surface and how it relates to the roaming mechanism would significantly further our understanding of the underlining mechanism. This can be done by pump-probe schemes using infrared radiation to access the vibrational frequencies, or high time-resolution to capture the charge migration. Understanding could then lead to controlling it, opening new chemical reaction possibilities.

References

[1] N. Bohr. I. on the constitution of atoms and molecules. *The London, Edinburgh, and Dublin Philosophical Magazine and Journal of Science*, 26(151):1–25, 1913. doi: 10.1080/14786441308634955. URL https://doi.org/10.1080/14786441308634955.

[2] E. Schrödinger. An undulatory theory of the mechanics of atoms and molecules. *Phys. Rev.*, 28:1049–1070, 12 1926. doi: 10.1103/PhysRev.28.1049. URL https://link.aps.org/doi/10.1103/PhysRev.28.1049.

[3] A. Einstein. Über einen die Erzeugung und Verwandlung des Lichtes betreffenden heuristischen Gesichtspunkt. *Annalen der Physik*, 322(6):132–148, 1905. doi: https://doi.org/10.1002/andp.19053220607. URL https://onlinelibrary.wiley.com/doi/abs/10.1002/andp.19053220607.

[4] P. Auger. Sur les rayons β secondaires produits dans un gaz par des rayons x. *C.R.A.S.*, 177:169–171, 1923.

[5] Lise Meitner. Über die Entstehung der β-Strahl-Spektren radioaktiver Substanzen. *Zeitschrift für Physik*, 9(1):131–144, 12 1922. doi: 10.1007/BF01326962. URL https://doi.org/10.1007/BF01326962.

[6] D. Townsend, S. A. Lahankar, S. K. Lee, S. D. Chambreau, A. G. Suits, X. Zhang, J. Rheinecker, L. B. Harding, and J. M. Bowman. The roaming atom: Straying from the reaction path in formaldehyde decomposition. *Science*, 306:1158–1161, 2004. doi: https://doi.org/10.1126/science.1104386.

[7] M. Joel Bowman and G. Arthur Suits. Roaming reactions: The third way. *Phys. Today*, 64:33–37, 11 2011. doi: 10.1063/PT.3.1330. URL https://doi.org/10.1063/PT.3.1330.

[8] P. L. Houston and S. H. Kable. Photodissociation of acetaldehyde as a second example of the roaming mechanism. *Proc. Natl. Acad. Sci. U. S. A.*, 103(44): 16079–16082, 2006. doi: 10.1073/pnas.0604441103.

[9] Brianna R. Heazlewood, Meredith J. T. Jordan, Scott H. Kable, Talitha M. Selby, David L. Osborn, Benjamin C. Shepler, Bastiaan J. Braams, and Joel M. Bowman. Roaming is the dominant mechanism for molecular products in acetaldehyde photodissociation. *Proc. Natl. Acad. Sci. U. S. A.*, 105(35):12719–12724, 2008. doi: 10.1073/pnas.0802769105.

[10] Satoshi Maeda, Koichi Ohno, and Keiji Morokuma. A theoretical study on the photodissociation of acetone: Insight into the slow intersystem crossing and exploration of nonadiabatic pathways to the ground state. *J. Phys. Chem. Lett.*, 1(12):1841–1845, 2010. doi: 10.1021/jz100551y.

[11] Michael P. Grubb, Michelle L. Warter, Hongyan Xiao, Satoshi Maeda, Keiji Morokuma, and Simon W. North. No straight path: Roaming in both ground- and excited-state photolytic channels of $no_3 \rightarrow no + o_2$. *Science*, 335(6072): 1075–1078, 2012. doi: 10.1126/science.1216911.

[12] Masaaki Nakamura, Po-Yu Tsai, Toshio Kasai, King-Chuen Lin, Federico Palazzetti, Andrea Lombardi, and Vincenzo Aquilanti. Dynamical, spectroscopic and computational imaging of bond breaking in photodissociation: roaming and role of conical intersections. *Faraday Discuss.*, 177:77–98, 2015. doi: 10.1039/C4FD00174E.

[13] Andrea Lombardi, Federico Palazzetti, Vincenzo Aquilanti, Hou-Kuan Li, Po-Yu Tsai, Toshio Kasai, and King-Chuen Lin. Rovibrationally excited molecules on the verge of a triple breakdown: Molecular and roaming mechanisms in the photodecomposition of methyl formate. *J. Phys. Chem. A*, 120(27):5155–5162, 2016. doi: 10.1021/acs.jpca.6b00723.

[14] Akshaya Kumar Rauta and Biswajit Maiti. Roaming mediated nonadiabatic dynamics in molecular hydrogen elimination from propane at 157nm. *Chem. Phys. Lett.*, 661:83–88, 2016. ISSN 0009-2614. doi: https://doi.org/10.1016/j.cplett.2016.08.057. URL `https://www.sciencedirect.com/science/article/pii/S0009261416306327`.

[15] Debadarshini Mishra, Juan Reino-González, Razib Obaid, Aaron C. LaForge, Sergio Díaz-Tendero, Fernando Martín, and Nora Berrah. Ultrafast molecular dynamics in ionized 1- and 2-propanol: from simple fragmentation to complex isomerization and roaming mechanisms. *Phys. Chem. Chem. Phys.*, 24:433–443, 2022. doi: 10.1039/D1CP04011A.

[16] Nagitha Ekanayake, Muath Nairat, Balram Kaderiya, Peyman Feizollah, Bethany Jochim, Travis Severt, Ben Berry, Kanaka Raju Pandiri, Kevin D. Carnes, Shashank Pathak, Daniel Rolles, Artem Rudenko, Itzik Ben-Itzhak, Christopher A. Mancuso, B. Scott Fales, James E. Jackson, Benjamin G. Levine,

and Marcos Dantus. Mechanisms and time-resolved dynamics for trihydrogen cation (h3+) formation from organic molecules in strong laser fields. *Sci. Rep.*, 7:4703, 2017. doi: 10.1038/s41598-017-04666-w.

[17] T Okino, Y Furukawa, P Liu, T Ichikawa, R Itakura, K Hoshina, K Yamanouchi, and H Nakano. Ejection dynamics of hydrogen molecular ions from methanol in intense laser fields. *J. Phys. B:At., Mol. Opt. Phys.*, 39(13):S515, 6 2006. doi: 10.1088/0953-4075/39/13/S24. URL `https://doi.org/10.1088/0953-4075/39/13/S24`.

[18] Joel M. Bowman and Paul L. Houston. Theories and simulations of roaming. *Chem. Soc. Rev.*, 46:7615–7624, 2017. doi: 10.1039/C7CS00578D. URL `http://dx.doi.org/10.1039/C7CS00578D`.

[19] Ignacio Fdez. Galván, Morgane Vacher, Ali Alavi, Celestino Angeli, Francesco Aquilante, Jochen Autschbach, Jie J. Bao, Sergey I. Bokarev, Nikolay A. Bogdanov, Rebecca K. Carlson, Liviu F. Chibotaru, Joel Creutzberg, Nike Dattani, Mickaël G. Delcey, Sijia S. Dong, Andreas Dreuw, Leon Freitag, Luis Manuel Frutos, Laura Gagliardi, Frédéric Gendron, Angelo Giussani, Leticia González, Gilbert Grell, Meiyuan Guo, Chad E. Hoyer, Marcus Johansson, Sebastian Keller, Stefan Knecht, Goran Kovačević, Erik Källman, Giovanni Li Manni, Marcus Lundberg, Yingjin Ma, Sebastian Mai, João Pedro Malhado, Per Åke Malmqvist, Philipp Marquetand, Stefanie A. Mewes, Jesper Norell, Massimo Olivucci, Markus Oppel, Quan Manh Phung, Kristine Pierloot, Felix Plasser, Markus Reiher, Andrew M. Sand, Igor Schapiro, Prachi Sharma, Christopher J. Stein, Lasse Kragh Sørensen, Donald G. Truhlar, Mihkel Ugandi, Liviu Ungur, Alessio Valentini, Steven Vancoillie, Valera Veryazov, Oskar Weser, Tomasz A. Wesołowski, Per-Olof Widmark, Sebastian Wouters, Alexander Zech, J. Patrick Zobel, and Roland Lindh. Openmolcas: From source code to insight. *Journal of Chemical Theory and Computation*, 15(11):5925–5964, 2019. doi: 10.1021/acs.jctc.9b00532. URL `https://doi.org/10.1021/acs.jctc.9b00532`. PMID: 31509407.

[20] Francesco Aquilante, Jochen Autschbach, Alberto Baiardi, Stefano Battaglia, Veniamin A. Borin, Liviu F. Chibotaru, Irene Conti, Luca De Vico, Mickaël Delcey, Ignacio Fdez. Galván, Nicolas Ferré, Leon Freitag, Marco Garavelli, Xuejun Gong, Stefan Knecht, Ernst D. Larsson, Roland Lindh, Marcus Lundberg, Per Åke Malmqvist, Artur Nenov, Jesper Norell, Michael Odelius, Massimo Olivucci, Thomas B. Pedersen, Laura Pedraza-González, Quan M. Phung, Kristine Pierloot, Markus Reiher, Igor Schapiro, Javier Segarra-Martí, Francesco Segatta, Luis Seijo, Saumik Sen, Dumitru-Claudiu Sergentu, Christopher J. Stein, Liviu Ungur, Morgane Vacher, Alessio Valentini, and Valera

Veryazov. Modern quantum chemistry with [open]molcas. *The Journal of Chemical Physics*, 152(21):214117, 06 2020. ISSN 0021-9606. doi: 10.1063/5.0004835. URL https://doi.org/10.1063/5.0004835.

[21] Giovanni Li Manni, Ignacio Fdez. Galván, Ali Alavi, Flavia Aleotti, Francesco Aquilante, Jochen Autschbach, Davide Avagliano, Alberto Baiardi, Jie J. Bao, Stefano Battaglia, Letitia Birnoschi, Alejandro Blanco-González, Sergey I. Bokarev, Ria Broer, Roberto Cacciari, Paul B. Calio, Rebecca K. Carlson, Rafael Carvalho Couto, Luis Cerdán, Liviu F. Chibotaru, Nicholas F. Chilton, Jonathan Richard Church, Irene Conti, Sonia Coriani, Juliana Cuéllar-Zuquin, Razan E. Daoud, Nike Dattani, Piero Decleva, Coen de Graaf, Mickaël G. Delcey, Luca De Vico, Werner Dobrautz, Sijia S. Dong, Rulin Feng, Nicolas Ferré, Michael Filatov(Gulak), Laura Gagliardi, Marco Garavelli, Leticia González, Yafu Guan, Meiyuan Guo, Matthew R. Hennefarth, Matthew R. Hermes, Chad E. Hoyer, Miquel Huix-Rotllant, Vishal Kumar Jaiswal, Andy Kaiser, Danil S. Kaliakin, Marjan Khamesian, Daniel S. King, Vladislav Kochetov, Marek Krośnicki, Arpit Arun Kumaar, Ernst D. Larsson, Susi Lehtola, Marie-Bernadette Lepetit, Hans Lischka, Pablo López Ríos, Marcus Lundberg, Dongxia Ma, Sebastian Mai, Philipp Marquetand, Isabella C. D. Merritt, Francesco Montorsi, Maximilian Mörchen, Artur Nenov, Vu Ha Anh Nguyen, Yoshio Nishimoto, Meagan S. Oakley, Massimo Olivucci, Markus Oppel, Daniele Padula, Riddhish Pandharkar, Quan Manh Phung, Felix Plasser, Gerardo Raggi, Elisa Rebolini, Markus Reiher, Ivan Rivalta, Daniel Roca-Sanjuán, Thies Romig, Arta Anushirwan Safari, Aitor Sánchez-Mansilla, Andrew M. Sand, Igor Schapiro, Thais R. Scott, Javier Segarra-Martí, Francesco Segatta, Dumitru-Claudiu Sergentu, Prachi Sharma, Ron Shepard, Yinan Shu, Jakob K. Staab, Tjerk P. Straatsma, Lasse Kragh Sørensen, Bruno Nunes Cabral Tenorio, Donald G. Truhlar, Liviu Ungur, Morgane Vacher, Valera Veryazov, Torben Arne Voß, Oskar Weser, Dihua Wu, Xuchun Yang, David Yarkony, Chen Zhou, J. Patrick Zobel, and Roland Lindh. The openmolcas web: A community-driven approach to advancing computational chemistry. *Journal of Chemical Theory and Computation*, 19(20):6933–6991, 2023. doi: 10.1021/acs.jctc.3c00182. URL https://doi.org/10.1021/acs.jctc.3c00182. PMID: 37216210.

[22] Björn O. Roos, Roland Lindh, Per-Åke Malmqvist, Valera Veryazov, and Per-Olof Widmark. Main group atoms and dimers studied with a new relativistic ano basis set. *The Journal of Physical Chemistry A*, 108(15):2851–2858, 2004. doi: 10.1021/jp031064+. URL https://doi.org/10.1021/jp031064+.

[23] Marvin Douglas and Norman M Kroll. Quantum electrodynamical corrections to the fine structure of helium. *Annals of Physics*, 82(1):89–

155, 1974. ISSN 0003-4916. doi: https://doi.org/10.1016/0003-4916(74)90333-9. URL https://www.sciencedirect.com/science/article/pii/0003491674903339.

[24] A. D. Becke. Density-functional exchange-energy approximation with correct asymptotic behavior. *Phys. Rev. A*, 38:3098–3100, Sep 1988. doi: 10.1103/PhysRevA.38.3098. URL https://link.aps.org/doi/10.1103/PhysRevA.38.3098.

[25] Hans Jørgen Aa. Jensen, Poul Jørgensen, and Hans Ågren. Efficient optimization of large scale mcscf wave functions with a restricted step algorithm. *The Journal of Chemical Physics*, 87(1):451–466, 07 1987. ISSN 0021-9606. doi: 10.1063/1.453590. URL https://doi.org/10.1063/1.453590.

[26] Per Åke. Malmqvist, Alistair. Rendell, and Björn O. Roos. The restricted active space self-consistent-field method, implemented with a split graph unitary group approach. *The Journal of Physical Chemistry*, 94(14):5477–5482, 1990. doi: 10.1021/j100377a011. URL https://doi.org/10.1021/j100377a011.

[27] Hans Ågren, A Flores-Riveros, Hans Jørgen, and Aa Jensen. An efficient method for calculating molecular radiative intensities in the vuv and soft x-ray wavelength regions. *Physica Scripta*, 40(6):745, dec 1989. doi: 10.1088/0031-8949/40/6/008. URL https://doi.org/10.1088/0031-8949/40/6/008.

[28] Per Åke Malmqvist, Kristine Pierloot, Abdul Rehaman Moughal Shahi, Christopher J. Cramer, and Laura Gagliardi. The restricted active space followed by second-order perturbation theory method: Theory and application to the study of cu2 and cu2o2 systems. *The Journal of Chemical Physics*, 128(20):204109, 05 2008. ISSN 0021-9606. doi: 10.1063/1.2920188. URL https://doi.org/10.1063/1.2920188.

[29] Vicenta Sauri, Luis Serrano-Andrés, Abdul Rehaman Moughal Shahi, Laura Gagliardi, Steven Vancoillie, and Kristine Pierloot. Multiconfigurational second-order perturbation theory restricted active space (raspt2) method for electronic excited states: A benchmark study. *Journal of Chemical Theory and Computation*, 7(1):153–168, 2011. doi: 10.1021/ct100478d. URL https://doi.org/10.1021/ct100478d. PMID: 26606229.

[30] Roland Lindh, Anders Bernhardsson, Gunnar Karlström, and Per Åke Malmqvist. On the use of a hessian model function in molecular geometry optimizations. *Chemical Physics Letters*, 241(4):423–428, 1995. ISSN 0009-2614. doi: https://doi.org/10.1016/0009-2614(95)00646-L. URL https://www.sciencedirect.com/science/article/pii/000926149500646L.

[31] Per Åke Malmqvist and Björn O. Roos. The casscf state interaction method. *Chemical Physics Letters*, 155(2):189–194, 1989. ISSN 0009-2614. doi: https://doi.org/10.1016/0009-2614(89)85347-3. URL https://www.sciencedirect.com/science/article/pii/0009261489853473.

[32] Per Åke Malmqvist, Björn O. Roos, and Bernd Schimmelpfennig. The restricted active space (ras) state interaction approach with spin–orbit coupling. *Chemical Physics Letters*, 357(3):230–240, 2002. ISSN 0009-2614. doi: https://doi.org/10.1016/S0009-2614(02)00498-0. URL https://www.sciencedirect.com/science/article/pii/S0009261402004980.

[33] Mickael G. Delcey, Lasse Kragh Sørensen, Morgane Vacher, Rafael C. Couto, and Marcus Lundberg. Efficient calculations of a large number of highly excited states for multiconfigurational wavefunctions. *Journal of Computational Chemistry*, 40(19):1789–1799, 2019. doi: https://doi.org/10.1002/jcc.25832. URL https://onlinelibrary.wiley.com/doi/abs/10.1002/jcc.25832.

[34] W. C. Röntgen. On a new kind of rays. *Nature*, 53:274–276, 1896. ISSN 1369. doi: 10.1038/053274b0. URL https://doi.org/10.1038/053274b0.

[35] A. Liénard. Champ électrique et magnétique produit par une charge concentrée en un point et animée d'un mouvement quelconque. *L'Éclairage Électrique*, 16, 1898.

[36] E. Wiechert. Elektrodynamische elementargesetze. *Annalen der Physik*, 309(4):667–689, 1901. doi: https://doi.org/10.1002/andp.19013090403. URL https://onlinelibrary.wiley.com/doi/abs/10.1002/andp.19013090403.

[37] Alexei Preobrajenski, Alexander Generalov, Gunnar Öhrwall, Maxim Tchaplyguine, Hamed Tarawneh, Stephan Appelfeller, Eleanor Frampton, and Noelle Walsh. FlexPES: a versatile soft X-ray beamline at MAXIV Laboratory. *Journal of Synchrotron Radiation*, 30(4):831–840, Jul 2023. doi: 10.1107/S1600577523003429. URL https://doi.org/10.1107/S1600577523003429.

[38] R. Pärna, R. Sankari, E. Kukk, E. Nõmmiste, M. Valden, M. Lastusaari, K. Kooser, K. Kokko, M. Hirsimäki, S. Urpelainen, P. Turunen, A. Kivimäki, V. Pankratov, L. Reisberg, F. Hennies, H. Tarawneh, R. Nyholm, and M. Huttula. FinEstBeaMS – A wide-range Finnish-Estonian Beamline for Materials Science at the 1.5 GeV storage ring at the MAX IV Laboratory. *Nuclear Instruments and Methods in Physics Research Section A: Accelerators, Spec-*

trometers, Detectors and Associated Equipment, 859:83–89, 2017. ISSN 0168-9002. doi: https://doi.org/10.1016/j.nima.2017.04.002. URL https://www.sciencedirect.com/science/article/pii/S0168900217304230.

[39] R Ovsyannikov and T Lau. The variable polarization undulator beamline ue52 pgm nanocluster trap at bessy ii. *Journal of large-scale research facilities*, 3(A105), 2 2017. doi: 10.17815/jlsrf-3-142. URL https://doi.org/10.17815/jlsrf-3-142.

[40] K Hirsch, J T Lau, Ph Klar, A Langenberg, J Probst, J Rittmann, M Vogel, V Zamudio-Bayer, T Möller, and B von Issendorff. X-ray spectroscopy on size-selected clusters in an ion trap: from the molecular limit to bulk properties. *Journal of Physics B: Atomic, Molecular and Optical Physics*, 42(15):154029, 7 2009. doi: 10.1088/0953-4075/42/15/154029. URL https://doi.org/10.1088/0953-4075/42/15/154029.

[41] Wolfgang Paul and Helmut Steinwedel. Notizen: Ein neues massenspektrometer ohne magnetfeld. *Zeitschrift für Naturforschung A*, 8(7):448–450, 7 1953. doi: 10.1515/zna-1953-0710. URL https://doi.org/10.1515/zna-1953-0710.

[42] Wolfgang Paul. Electromagnetic traps for charged and neutral particles. *Rev. Mod. Phys.*, 62:531–540, Jul 1990. doi: 10.1103/RevModPhys.62.531. URL https://link.aps.org/doi/10.1103/RevModPhys.62.531.

[43] Joachim Stöhr. Nexafs spectroscopy. *Springer Berlin, Heidelberg*, 1992. doi: 10.1007/978-3-662-02853-7.

[44] S. Svensson, J. O. Forsell, H. Siegbahn, A. Ausmees, G. Bray, S. Södergren, S. Sundin, S. J. Osborne, S. Aksela, E. Nõmmiste, J. Jauhiainen, M. Jurvansuu, J. Karvonen, P. Barta, W. R. Salaneck, A. Evaldsson, M. Lögdlund, and A. Fahlman. New end station for the study of gases, liquids, and solid films at the MAX laboratory. *Review of Scientific Instruments*, 67(6):2149–2156, 06 1996. ISSN 0034-6748. doi: 10.1063/1.1147029. URL https://doi.org/10.1063/1.1147029.

[45] Joseph Ladislas Wiza. Microchannel plate detectors. *Nuclear Instruments and Methods*, 162(1):587–601, 1979. ISSN 0029-554X. doi: https://doi.org/10.1016/0029-554X(79)90734-1. URL https://www.sciencedirect.com/science/article/pii/0029554X79907341.

[46] J.H.D. Eland. The dynamics of three-body dissociations of dications studied by the triple coincidence technique pepipico. *Molecular Physics*, 61(3):725–745,

1987. doi: 10.1080/00268978700101421. URL https://doi.org/10.1080/00268978700101421.

[47] Kuno Kooser, Antti Kivimäki, Paavo Turunen, Rainer Pärna, Liis Reisberg, Marco Kirm, Mika Valden, Marko Huttula, and Edwin Kukk. Gas-phase endstation of electron, ion and coincidence spectroscopies for diluted samples at the FinEstBeAMS beamline of the MAXIV 1.5GeV storage ring. *Journal of Synchrotron Radiation*, 27(4):1080–1091, 7 2020. doi: 10.1107/S1600577520007146. URL https://doi.org/10.1107/S1600577520007146.

[48] W. C. Wiley and I. H. McLaren. Time-of-flight mass spectrometer with improved resolution. *Review of Scientific Instruments*, 26(12):1150–1157, 12 1955. ISSN 0034-6748. doi: 10.1063/1.1715212. URL https://doi.org/10.1063/1.1715212.

[49] S.E. Sobottka and M.B. Williams. Delay line readout of microchannel plates. *IEEE Transactions on Nuclear Science*, 35(1):348–351, 1988. doi: 10.1109/23.12740.

[50] O Jagutzki, V Mergel, K Ullmann-Pfleger, L Spielberger, U Spillmann, R Dörner, and H Schmidt-Böcking. A broad-application microchannel-plate detector system for advanced particle or photon detection tasks: large area imaging, precise multi-hit timing information and high detection rate. *Nuclear Instruments and Methods in Physics Research Section A: Accelerators, Spectrometers, Detectors and Associated Equipment*, 477(1):244–249, 2002. ISSN 0168-9002. doi: https://doi.org/10.1016/S0168-9002(01)01839-3. URL https://www.sciencedirect.com/science/article/pii/S0168900201018393. 5th Int. Conf. on Position-Sensitive Detectors.

[51] Roentdek. Hexagonal delay line detectors, 2026. https://www.roentdek.com/detectors [Accessed: 2026-02-20].

[52] Roentdek. Delay line detectors (). *IEEE Transactions on Nuclear Science*, 35(1):348–351, 1988. doi: 10.1109/23.12740.

[53] R. Dörner, V. Mergel, O. Jagutzki, L. Spielberger, J. Ullrich, R. Moshammer, and H. Schmidt-Böcking. Cold target recoil ion momentum spectroscopy: a 'momentum microscope' to view atomic collision dynamics. *Physics Reports*, 330(2):95–192, 2000. ISSN 0370-1573. doi: https://doi.org/10.1016/S0370-1573(99)00109-X. URL https://www.sciencedirect.com/science/article/pii/S037015739900109X.

[54] R. Lindblad, L. Kjellsson, R. C. Couto, M. Timm, C. Bülow, V. Zamudio-Bayer, M. Lundberg, B. von Issendorff, J. T. Lau, S. L. Sorensen, V. Carravetta,

H. Ågren, and J.-E. Rubensson. X-ray absorption spectrum of the n_2^+ molecular ion. *Phys. Rev. Lett.*, 124:203001, 5 2020. doi: 10.1103/PhysRevLett.124.203001. URL https://link.aps.org/doi/10.1103/PhysRevLett.124.203001.

[55] Lucas M. Cornetta, Ludvig Kjellsson, Rafael C. Couto, Hans Ågren, Vincenzo Carravetta, Stacey L. Sorensen, Markus Kubin, Christine Bülow, Vicente Zamudio-Bayer, Bernd von Issendorff, J. Tobias Lau, Johan Söderström, Marcus Agåker, Jan-Erik Rubensson, and Rebecka Lindblad. X-ray-absorption spectrum of O_2^+. *Phys. Rev. A*, 111:022808, 2 2025. doi: 10.1103/PhysRevA.111.022808. URL https://link.aps.org/doi/10.1103/PhysRevA.111.022808.

[56] Rafael C. Couto, Ludvig Kjellsson, Hans Ågren, Vincenzo Carravetta, Stacey L. Sorensen, Markus Kubin, Christine Bülow, Martin Timm, Vicente Zamudio-Bayer, Bernd von Issendorff, J. Tobias Lau, Johan Söderström, Jan-Erik Rubensson, and Rebecka Lindblad. The carbon and oxygen K-edge NEXAFS spectra of CO+. *Phys. Chem. Chem. Phys.*, 22:16215–16223, 2020. doi: 10.1039/D0CP02207A. URL http://dx.doi.org/10.1039/D0CP02207A.

[57] Rebecka Lindblad, Ludvig Kjellsson, Emiliano De Santis, Vicente Zamudio-Bayer, Bernd von Issendorff, Stacey L. Sorensen, J. Tobias Lau, Weijie Hua, Vincenzo Carravetta, Jan-Erik Rubensson, Hans Ågren, and Rafael C. Couto. Experimental and theoretical near-edge x-ray-absorption fine-structure studies of no^+. *Phys. Rev. A*, 106:042814, 10 2022. doi: 10.1103/PhysRevA.106.042814. URL https://link.aps.org/doi/10.1103/PhysRevA.106.042814.

[58] Rafael C. Couto, Weijie Hua, Rebecka Lindblad, Ludvig Kjellsson, Stacey L. Sorensen, Markus Kubin, Christine Bülow, Martin Timm, Vicente Zamudio-Bayer, Bernd von Issendorff, Johan Söderström, J. Tobias Lau, Jan-Erik Rubensson, Hans Ågren, and Vincenzo Carravetta. Breaking inversion symmetry by protonation: experimental and theoretical nexafs study of the diazynium ion, n2h+. *Phys. Chem. Chem. Phys.*, 23:17166–17176, 2021. doi: 10.1039/D1CP02002A. URL http://dx.doi.org/10.1039/D1CP02002A.

[59] R. B. Sharma, N. M. Semo, and W. S. Koski. Dynamics of the reactions of methylium, methylene radical cation, and methyliumylidene with acetylene. *The Journal of Physical Chemistry*, 91(15):4127–4131, 1987. doi: 10.1021/j100299a037. URL https://doi.org/10.1021/j100299a037.

[60] C.N. Keller, V.G. Anicich, and T.E. Cravens. Model of titans ionosphere with detailed hydrocarbon ion chemistry. *Planetary and Space Science*, 46(9):1157–1174, 1998. ISSN 0032-0633. doi: https://doi.org/10.1016/S0032-0633(98)

00053-1. URL https://www.sciencedirect.com/science/article/pii/S0032063398000531.

[61] A. G. G. M. Tielens. The molecular universe. *Rev. Mod. Phys.*, 85:1021–1081, 7 2013. doi: 10.1103/RevModPhys.85.1021. URL https://link.aps.org/doi/10.1103/RevModPhys.85.1021.

[62] D W Savin, N S Brickhouse, J J Cowan, R P Drake, S R Federman, G J Ferland, A Frank, M S Gudipati, W C Haxton, E Herbst, S Profumo, F Salama, L M Ziurys, and E G Zweibel. The impact of recent advances in laboratory astrophysics on our understanding of the cosmos. *Reports on Progress in Physics*, 75(3):036901, 2 2012. doi: 10.1088/0034-4885/75/3/036901. URL https://doi.org/10.1088/0034-4885/75/3/036901.

[63] A S Schlachter, M M Sant'Anna, A M Covington, A Aguilar, M F Gharaibeh, E D Emmons, S W J Scully, R A Phaneuf, G Hinojosa, I Álvarez, C Cisneros, A Müller, and B M McLaughlin. Lifetime of a K-shell vacancy in atomic carbon created by 1s $\rightarrow$ 2p photoexcitation of C+. *Journal of Physics B: Atomic, Molecular and Optical Physics*, 37(5):L103, 2 2004. doi: 10.1088/0953-4075/37/5/L03. URL https://doi.org/10.1088/0953-4075/37/5/L03.

[64] A. Müller, A. Borovik, T. Buhr, J. Hellhund, K. Holste, A. L. D. Kilcoyne, S. Klumpp, M. Martins, S. Ricz, J. Viefhaus, and S. Schippers. Observation of a four-electron auger process in near-k-edge photoionization of singly charged carbon ions. *Phys. Rev. Lett.*, 114:013002, 1 2015. doi: 10.1103/PhysRevLett.114.013002. URL https://link.aps.org/doi/10.1103/PhysRevLett.114.013002.

[65] J. M. Bizau, D. Cubaynes, S. Guilbaud, M. M. Al Shorman, M. F. Gharaibeh, I. Q. Ababneh, C. Blancard, and B. M. McLaughlin. K-shell photoionization of O^+ and O^{2+} ions: Experiment and theory. *Phys. Rev. A*, 92:023401, 8 2015. doi: 10.1103/PhysRevA.92.023401. URL https://link.aps.org/doi/10.1103/PhysRevA.92.023401.

[66] M. F. Hasoglu, Sh. A. Abdel-Naby, T. W. Gorczyca, J. J. Drake, and B. M. McLaughlin. K-shell photoabsorption studies of the carbon isonuclear sequence. *The Astrophysical Journal*, 724(2):1296, 11 2010. doi: 10.1088/0004-637X/724/2/1296. URL https://doi.org/10.1088/0004-637X/724/2/1296.

[67] J.-P. Mosnier, E. T. Kennedy, P. van Kampen, D. Cubaynes, S. Guilbaud, N. Sisourat, A. Puglisi, S. Carniato, and J.-M. Bizau. Inner-shell photoexcitations as probes of the molecular ions CH^+, oh^+, and sih^+: Measurements

and theory. *Phys. Rev. A*, 93:061401, 6 2016. doi: 10.1103/PhysRevA.93.061401. URL https://link.aps.org/doi/10.1103/PhysRevA.93.061401.

[68] A. Müller, A. Borovik, T. Buhr, J. Hellhund, K. Holste, A. L. D. Kilcoyne, S. Klumpp, M. Martins, S. Ricz, J. Viefhaus, and S. Schippers. Near-K-edge single, double, and triple photoionization of C^+ ions. *Phys. Rev. A*, 97:013409, 1 2018. doi: 10.1103/PhysRevA.97.013409. URL https://link.aps.org/doi/10.1103/PhysRevA.97.013409.

[69] A. Müller, A. Borovik, K. Holste, S. Klumpp, M. Martins, and S. Schippers. Near-K-edge single and double photoionization of C^{2+} ions. *Phys. Rev. A*, 107: 032806, 3 2023. doi: 10.1103/PhysRevA.107.032806. URL https://link.aps.org/doi/10.1103/PhysRevA.107.032806.

[70] M. Alagia, M. Lavollée, R. Richter, U. Ekström, V. Carravetta, D. Stranges, B. Brunetti, and S. Stranges. Probing the potential energy surface by high-resolution x-ray absorption spectroscopy: The umbrella motion of the core-excited CH_3 free radical. *Phys. Rev. A*, 76:022509, 8 2007. doi: 10.1103/PhysRevA.76.022509. URL https://link.aps.org/doi/10.1103/PhysRevA.76.022509.

[71] U. Ekström, V. Carravetta, M. Alagia, M. Lavollée, R. Richter, C. Bolcato, and S. Stranges. The umbrella motion of core-excited CH3 and CD3 methyl radicals. *The Journal of Chemical Physics*, 128(4):044302, 01 2008. ISSN 0021-9606. doi: 10.1063/1.2822246. URL https://doi.org/10.1063/1.2822246.

[72] W. Heisenberg. Über den anschaulichen Inhalt der quantentheoretischen Kinematik und Mechanik. *Zeitschrift für Physik*, 43(3):172–198, 3 1927. doi: 10.1007/BF01397280. URL https://doi.org/10.1007/BF01397280.

[73] Oskar Asvany, Padma Kumar P, Britta Redlich, Ilka Hegemann, Stephan Schlemmer, and Dominik Marx. Understanding the infrared spectrum of bare CH_5^+. *Science*, 309(5738):1219–1222, 2005. doi: 10.1126/science.1113729. URL https://www.science.org/doi/abs/10.1126/science.1113729.

[74] Oskar Asvany, Koichi M. T. Yamada, Sandra Brünken, Alexey Potapov, and Stephan Schlemmer. Experimental ground-state combination differences of CH_5^+. *Science*, 347(6228):1346–1349, 2015. doi: 10.1126/science.aaa3304. URL https://www.science.org/doi/abs/10.1126/science.aaa3304.

[75] W. Eberhardt, T. K. Sham, R. Carr, S. Krummacher, M. Strongin, S. L. Weng, and D. Wesner. Site-specific fragmentation of small molecules following soft-x-ray excitation. *Phys. Rev. Lett.*, 50:1038–1041, Apr 1983. doi: 10.

1103/PhysRevLett.50.1038. URL https://link.aps.org/doi/10.1103/PhysRevLett.50.1038.

[76] M. C. Nelson, J. Murakami, S. L. Anderson, and D. M. Hanson. Fragmentation of acetone following excitation in the region of the oxygen K edge. *The Journal of Chemical Physics*, 86(8):4442–4445, 04 1987. ISSN 0021-9606. doi: 10.1063/1.452717. URL https://doi.org/10.1063/1.452717.

[77] X. J. Liu, G. Prümper, E. Kukk, R. Sankari, M. Hoshino, C. Makochekanwa, M. Kitajima, H. Tanaka, H. Yoshida, Y. Tamenori, and K. Ueda. Site-selective ion production of the core-excited CH_3F molecule probed by Auger-electron–ion coincidence measurements. *Phys. Rev. A*, 72:042704, 10 2005. doi: 10.1103/PhysRevA.72.042704. URL https://link.aps.org/doi/10.1103/PhysRevA.72.042704.

[78] S. Nagaoka, G. Prümper, H. Fukuzawa, M. Hino, M. Takemoto, Y. Tamenori, J. Harries, I. H. Suzuki, O. Takahashi, K. Okada, K. Tabayashi, X.-J. Liu, T. Lischke, and K. Ueda. Electron-ion-ion triple-coincidence spectroscopic study of site-specific fragmentation caused by Si:2p core-level photoionization of $F_3SiCH_2CH_2Si(CH_3)_3$ vapor. *Phys. Rev. A*, 75:020502, 2 2007. doi: 10.1103/PhysRevA.75.020502. URL https://link.aps.org/doi/10.1103/PhysRevA.75.020502.

[79] W C Stolte, G Öhrwall, M M Sant'Anna, I Dominguez Lopez, L T N Dang, M N Piancastelli, and D W Lindle. 100% site-selective fragmentation in core-hole-photoexcited methanol by anion-yield spectroscopy. *Journal of Physics B: Atomic, Molecular and Optical Physics*, 35(12):L253, 6 2002. doi: 10.1088/0953-4075/35/12/102. URL https://doi.org/10.1088/0953-4075/35/12/102.

[80] C. Miron, M. Simon, N. Leclercq, D. L. Hansen, and P. Morin. Site-selective photochemistry of core excited molecules: Role of the internal energy. *Phys. Rev. Lett.*, 81:4104–4107, 11 1998. doi: 10.1103/PhysRevLett.81.4104. URL https://link.aps.org/doi/10.1103/PhysRevLett.81.4104.

[81] E. Itälä, D.T. Ha, K. Kooser, M.A. Huels, E. Rachlew, E. Nõmmiste, U. Joost, and E. Kukk. Molecular fragmentation of pyrimidine derivatives following site-selective carbon core ionization. *Journal of Electron Spectroscopy and Related Phenomena*, 184(3):119–124, 2011. ISSN 0368-2048. doi: https://doi.org/10.1016/j.elspec.2011.01.007. URL https://www.sciencedirect.com/science/article/pii/S0368204811000132. Advances in Vacuum Ultraviolet and X-ray Physics.

[82] K. Sigbahn. *ESCA, Atomic, Molecular and Solid State Structure Studiedby Means of Electron Spetroscopy*. Almquist & Wiksells Boktryckeri, 1967.

[83] H. Iwayama, N. Sisourat, P. Lablanquie, F. Penent, J. Palaudoux, L. Andric, J. H. Eland, K. Bučar, M. Žitnik, Y. Velkov, Y. Hikosaka, M. Nakano, and E. Shigemasa. A local chemical environment effect in site-specific auger spectra of ethyl trifluoroacetate. *The Journal of chemical physics*, 138, 2013. doi: 10.1063/1.4773294. URL https://doi.org/10.1063/1.4773294.

[84] Ludger Inhester, Bart Oostenrijk, Minna Patanen, Esko Kokkonen, Stephen H. Southworth, Christoph Bostedt, Oksana Travnikova, Tatiana Marchenko, Sang-Kil Son, Robin Santra, Marc Simon, Linda Young, and Stacey L. Sorensen. Chemical understanding of the limited site-specificity in molecular inner-shell photofragmentation. *The Journal of Physical Chemistry Letters*, 9(5):1156–1163, 2018. doi: 10.1021/acs.jpclett.7b03235. URL https://doi.org/10.1021/acs.jpclett.7b03235. PMID: 29444399.

[85] S L Sorensen, X Zheng, S H Southworth, M Patanen, E Kokkonen, B Oostenrijk, O Travnikova, T Marchenko, M Simon, C Bostedt, G Doumy, L Cheng, and L Young. From synchrotrons for xfels: the soft x-ray near-edge spectrum of the esca molecule. *Journal of Physics B: Atomic, Molecular and Optical Physics*, 53(24):244011, dec 2020. doi: 10.1088/1361-6455/abc6bd. URL https://doi.org/10.1088/1361-6455/abc6bd.

[86] Sanghamitra Deb and Peter M. Weber. The ultrafast pathway of photon-induced electrocyclic ring-opening reactions: The case of 1,3-cyclohexadiene. *Annual Review of Physical Chemistry*, 62(Volume 62, 2011):19–39, 2011. ISSN 1545-1593. doi: https://doi.org/10.1146/annurev.physchem.012809.103350. URL https://www.annualreviews.org/content/journals/10.1146/annurev.physchem.012809.103350.

[87] Brenden C. Arruda and Roseanne J. Sension. Ultrafast polyene dynamics: the ring opening of 1,3-cyclohexadiene derivatives. *Phys. Chem. Chem. Phys.*, 16:4439–4455, 2014. doi: 10.1039/C3CP54767A. URL http://dx.doi.org/10.1039/C3CP54767A.

[88] K. Kimura, S. Katsumata, Y. Achiba, T. Yamazaki, and S. Iwata. *Handbook of He(I) photoelectron spectra of fundamental organic molecules*. Japan Scientific Societies Press, 1981.

[89] Vladimir S. Petrović, Marco Siano, James L. White, Nora Berrah, Christoph Bostedt, John D. Bozek, Douglas Broege, Max Chalfin, Ryan N. Coffee, James Cryan, Li Fang, Joseph P. Farrell, Leszek J Frasinski, James M. Glownia, Markus

Gühr, Matthias Hoener, David M. P. Holland, Jaehee Kim, Jonathan P. Marangos, Todd Martinez, Brian K. McFarland, Russell S. Minns, Shungo Miyabe, Sebastian Schorb, Roseanne J. Sension, Limor S. Spector, Richard Squibb, Hongli Tao, Jonathan G. Underwood, and Philip H. Bucksbaum. Transient x-ray fragmentation: Probing a prototypical photoinduced ring opening. *Phys. Rev. Lett.*, 108:253006, Jun 2012. doi: 10.1103/PhysRevLett.108.253006. URL https://link.aps.org/doi/10.1103/PhysRevLett.108.253006.

[90] Yibo Lei, Huiyu Wu, Xiaolei Zheng, Gaohong Zhai, and Chaoyuan Zhu. Photo-induced 1,3-cyclohexadiene ring opening reaction: Ab initio on-the-fly nonadiabatic molecular dynamics simulation. *Journal of Photochemistry and Photobiology A: Chemistry*, 317:39–49, 2016. ISSN 1010-6030. doi: https://doi.org/10.1016/j.jphotochem.2015.10.025. URL https://www.sciencedirect.com/science/article/pii/S1010603015300071.

[91] Robert J. Buenker and Sigrid D. Peyerimhoff. Theoretical study of the geometry, reactivity, and spectrum of cyclopropane. *The Journal of Physical Chemistry*, 73 (5):1299–1313, 1969. doi: 10.1021/j100725a022. URL https://doi.org/10.1021/j100725a022.

[92] Shabnam Oghbaie, Mathieu Gisselbrecht, Erik P. Månsson, Joakim Laksman, Christian Stråhlman, Anna Sankari, and Stacey L. Sorensen. Dissociation of cyclopropane in double ionization continuum. *Phys. Chem. Chem. Phys.*, 19: 19631–19639, 2017. doi: 10.1039/C7CP01667K. URL http://dx.doi.org/10.1039/C7CP01667K.

[93] J.A. Tossell, J.H. Moore, and M.A. Coplan. Molecular distortions and electron momentum distributions. *Chemical Physics Letters*, 67(2):356–358, 1979. ISSN 0009-2614. doi: https://doi.org/10.1016/0009-2614(79)85177-5. URL https://www.sciencedirect.com/science/article/pii/0009261479851775.

[94] P.R. Keller, J.W. Taylor, Thomas A. Carlson, T.A. Whitley, and F.A. Grimm. Angle-resolved photoelectron spectroscopy of cyclopropane. *Chemical Physics*, 99(2):317–321, 1985. ISSN 0301-0104. doi: https://doi.org/10.1016/0301-0104(85)80128-2. URL https://www.sciencedirect.com/science/article/pii/0301010485801282.

[95] Zhongjun Li, Xiangjun Chen, Xu Shan, Tao Liu, and Kezun Xu. Electron momentum spectroscopy study of jahn–teller effect in cyclopropane. *The Journal of Chemical Physics*, 130(5):054302, 02 2009. ISSN 0021-9606. doi: 10.1063/1.3068619. URL https://doi.org/10.1063/1.3068619.

[96] A. P. Hitchcock, D. C. Newbury, I. Ishii, J. Stöhr, J. A. Horsley, R. D. Redwing, A. L. Johnson, and F. Sette. Carbon K⊠shell excitation of gaseous and condensed cyclic hydrocarbons: C3H6, C4H8, C5H8, C5H1, C6H1, C6H12, and C8H8. *The Journal of Chemical Physics*, 85(9):4849–4862, 11 1986. ISSN 0021-9606. doi: 10.1063/1.451719. URL https://doi.org/10.1063/1.451719.

[97] K.H. Sze and C.E. Brion. Inner-shell and valence-shell electronic excitation of cyclopropane and ethylene oxide by high resolution electron energy loss spectroscopy. *Journal of Electron Spectroscopy and Related Phenomena*, 57(2): 117–135, 1991. ISSN 0368-2048. doi: https://doi.org/10.1016/0368-2048(91)85019-P. URL https://www.sciencedirect.com/science/article/pii/036820489185019P.

[98] D. Duflot, S. Zeggari, and J.-P. Flament. Ab initio study of core excited cyclopropane. *Chemical Physics*, 327(2):518–528, 2006. ISSN 0301-0104. doi: https://doi.org/10.1016/j.chemphys.2006.05.027. URL https://www.sciencedirect.com/science/article/pii/S0301010406003168.

[99] Sung Kwon, Shawn Sandhu, Moaid Shaik, Jacob Stamm, Jesse Sandhu, Rituparna Das, Caitlin V. Hetherington, Benjamin G. Levine, and Marcos Dantus. What is the mechanism of H_3^+ formation from cyclopropane? *J. Phys. Chem. A*, 127(41):8633–8638, 2023. doi: 10.1021/acs.jpca.3c05442.

[100] J. Cooper and R. N. Zare. Photoelectron Angular Distributions. In *Lectures in Theoretical Physics: Atomic Collision Processes, Vol. XI-C*, pages 317–337. Gordon and Breach, 1969. URL https://jila.colorado.edu/publications/photoelectron-angular-distributions.

[101] Lucas Schwob, Simon Dörner, Kaan Atak, Kaja Schubert, Martin Timm, Christine Bülow, Vicente Zamudio-Bayer, Bernd von Issendorff, J. Tobias Lau, Simone Techert, and Sadia Bari. Site-selective dissociation upon sulfur l-edge x-ray absorption in a gas-phase protonated peptide. *The Journal of Physical Chemistry Letters*, 11(4):1215–1221, 2020. doi: 10.1021/acs.jpclett.0c00041. URL https://doi.org/10.1021/acs.jpclett.0c00041. PMID: 31978303.

[102] Debadarshini Mishra, Aaron C. LaForge, Lauren M. Gorman, Sergio Díaz-Tendero, Fernando Martín, and Nora Berrah. Direct tracking of H_2 roaming reaction in real time. *Nat. Commun.*, 15:6656, 2024. doi: 10.1038/s41467-024-49671-6.

[103] K Ueda, A De Fanis, N Saito, M Machida, K Kubozuka, H Chiba, Y Muramatu, Y Sato, A Czasch, O Jaguzki, R Dörner, A Cassimi, M Kitajima, T Furuta, H Tanaka, S.L Sorensen, K Okada, S Tanimoto, K Ikejiri,

Y Tamenori, H Ohashi, and I Koyano. Nuclear motion and symmetry breaking of the B 1s-excited BF_3 molecule. *Chem. Phys.*, 289(1):135–147, 2003. ISSN 0301-0104. doi: https://doi.org/10.1016/S0301-0104(02)00903-5. URL https://www.sciencedirect.com/science/article/pii/S0301010402009035. Decay Processes in Core-excited Species.

[104] J. Laksman, E. P. Månsson, C. Grunewald, A. Sankari, M. Gisselbrecht, D. Céolin, and S. L. Sorensen. Role of the Renner-teller effect after core hole excitation in the dissociation dynamics of carbon dioxide dication. *J. Chem. Phys.*, 136(10):104303, 03 2012. ISSN 0021-9606. doi: 10.1063/1.3692293. URL https://doi.org/10.1063/1.3692293.

[105] N. Neumann, D. Hant, L. Ph. H. Schmidt, J. Titze, T. Jahnke, A. Czasch, M. S. Schöffler, K. Kreidi, O. Jagutzki, H. Schmidt-Böcking, and R. Dörner. Fragmentation Dynamics of CO_2^{3+} Investigated by Multiple Electron Capture in Collisions with Slow Highly Charged Ions. *Phys. Rev. Lett.*, 104:103201, 3 2010. doi: 10.1103/PhysRevLett.104.103201. URL https://link.aps.org/doi/10.1103/PhysRevLett.104.103201.

[106] R. H. Dalitz. Decay of τ Mesons of Known Charge. *Phys. Rev.*, 94:1046–1051, 5 1954. doi: 10.1103/PhysRev.94.1046. URL https://link.aps.org/doi/10.1103/PhysRev.94.1046.

[107] Shizuka Hsieh and John H D Eland. Reaction dynamics of three-body dissociations in triatomic molecules from single-photon double ionization studied by a time- and position-sensitive coincidence method. *J. Phys. B:At., Mol. Opt. Phys.*, 30(20):4515, 10 1997. doi: 10.1088/0953-4075/30/20/015. URL https://doi.org/10.1088/0953-4075/30/20/015.

[108] T. Severt, Jyoti Rajput, Ben Berry, Bethany Jochim, Peyman Feizollah, Balram Kaderiya, M. Zohrabi, Farzaneh Ziaee, Kanaka Raju P., D. Rolles, A. Rudenko, K. D. Carnes, B. D. Esry, and I. Ben-Itzhak. Native frames: An approach for separating sequential and concerted three-body fragmentation. *Phys. Rev. A*, 110:053104, 11 2024. doi: 10.1103/PhysRevA.110.053104. URL https://link.aps.org/doi/10.1103/PhysRevA.110.053104.

[109] Irina I. Mizus, Oleg L. Polyansky, Laura K. McKemmish, Jonathan Tennyson, Alexander Alijah, and Nikolai F. Zobov. A global potential energy surface for h3+. *Molecular Physics*, 117(13):1663–1672, 2019. doi: 10.1080/00268976.2018.1554195. URL https://doi.org/10.1080/00268976.2018.1554195.

[110] K. Z. Lin, D. L. Guo, X. L. Zhu, D. M. Zhao, X. B. Zhu, X. Shan, S. F. Zhang, X. J. Chen, and X. Ma. Three-body fragmentation dynamics of the

cyclopropane trication following 5.8-MeV/u Ni^{19+} impact. *Phys. Rev. A*, 109: 022817, Feb 2024. doi: 10.1103/PhysRevA.109.022817. URL https://link.aps.org/doi/10.1103/PhysRevA.109.022817.

Printed by Media-Tryck, Lund 2026 NORDIC SWAN ECOLABEL 3041 0903

Division of Synchrotron Radiation Research
Department of Physics
Faculty of Science

ISBN 978-91-8104-951-0